What's the real role of iron-oxides in the optical properties of dust aerosols?

X. L. Zhang[1, 2], G. J. Wu[2], C. L. Zhang[3], T. L. Xu[2, 4], Q. Q. Zhou[1]

[1]Key laboratory of Wetland Ecology and Environment, Northeast Institute of Geography and Agroecology, Chinese Academy of Sciences, Changchun 130102, China

[2] Key Laboratory of Tibetan Environment Changes and Land Surface Processes, Institute of Tibetan Plateau Research, CAS Center for Excellence and Innovation in Tibetan Plateau Earth System Sciences, Chinese Academy of Sciences, Beijing 100101, China

[3] Research Center for Eco-Environmental Sciences, Chinese Academy of Sciences, Beijing, 100085, China

[4] University of Chinese Academy of Sciences, Beijing 100049, China

Correspondence to: X. L. Zhang (zhangxuelei@neigae.ac.cn) and G. J. Wu (wugj@itpcas.ac.cn)

Abstract:

Iron oxides compounds constitute an important component of mineral dust aerosol. Several previous studies have shown that these minerals are strong absorbers at visible wavelengths and thus that they play a critical role in the overall climate perturbation caused by dust aerosol. When compiling a database of complex refractive indices of possible mineral species of iron-oxides to study their optical properties, we found that uniformly continuous optical constants for a single type of iron-oxides in the wavelength range between 0.2 μm and 50 μm is very scarce and that the use of hematite to represent all molecular or mineral iron-oxides types is a popular hypothesis. However, the crucial problem is that three continuous datasets for complex refractive indices of hematite are employed in climate models, but there are significant differences between them. Thus, the real role of iron-oxides in the optical properties of dust aerosols becomes a key scientific question, and we address this problem by considering different refractive indices, size distributions, and more logical weight fractions and mixing states of hematite. Based on the microscopic observations, a semi-external mixture that employs an external mixture between Fe-aggregates and other minerals and partly internal mixing between iron-oxides and aluminosilicate particles is advised as the optimal approximation. The simulations demonstrate that hematite with a spectral refractive indices from Longtin et al. (1988) shows approximately equal absorbing capacity to the mineral illite over the whole wavelength region from 0.55 μm to 2.5 μm, and only enhances the optical absorption of aerosol mixture at $\lambda < 0.55$ um. Using the dataset from Querry (1985) may overestimate the optical absorption of hematite at both visible

and near-infrared wavelengths. More laboratory measurements of the refractive index of iron-oxides, especially for hematite and goethite in the visible spectrum, should therefore be taken into account when assessing the effect of mineral dust on climate forcing.

1. Introduction

Iron oxides in dusts are now identified as being important component for a number of climatic, environmental and biological processes. Over the past decade, iron-oxide minerals have been shown to be able to strongly absorb solar radiation (Tegen et al., 1997; Sokolik and Toon, 1999; Lafon et al., 2004; Qin and Mitchell, 2009; Redmond et al., 2010), and thus have a direct impact on the Earth's radiation balance (Balkanski et al., 2007; Scanza et al., 2015; Smith and Grainger, 2014). Based on the ability to absorb acidic gases and water vapor (Baltrusaitis et al., 2007; Wijenayaka et al., 2012; Song and Boily, 2013), iron oxides also contribute to heterogeneous reactions and cloud processes (Shi et al., 2011; Dupart et al., 2012), further influencing the radiation balance. In particular, layers of dust on snow and ice cover accelerate the melting of snow and ice by diminishing the surface albedo (Painter et al., 2010; Ginot et al., 2014) and the heat-absorbing properties of iron oxides in these dust layers can add to this effect (Kaspari et al., 2014; Reynolds et al., 2013; Dang and Hegg, 2014). Moreover, the deposited iron-bearing dust aerosols provide critical nutrients to marine and terrestrial ecosystems, which associated with consequential important drawdown of atmospheric carbon dioxide (Jickells et al., 2005; Shao et al., 2011; Nickovic et al., 2013). However, these effects can lead to either positive or negative net radiative perturbation depending mostly on the underlying surface albedo, vertical profile (optical depth and height of dust layer), particle size distribution and mineralogy (Liao and Seinfeld, 1998; Calquin et al., 1999). This large uncertainty results from our limited knowledge of the physical, chemical and optical properties of atmospheric iron oxides on various space and time scales (Tegen et al., 1997; Sokolik et al., 2001; Formenti et al., 2011).

The element iron can be found among numerous mineralogical species, such as feldspars, clays (e.g. illite, smectite, chlorite and biotite), iron-oxides, iron-hydroxides and so on. A useful mineralogical classification frequently used in soil science distinguishes two categories of iron: (i) "structural iron" (in either the Fe(II) or Fe(III) oxidation states), trapped in the crystal lattice of aluminosilicate minerals; and (ii) iron (in the Fe(III) oxidation state), in the form of discrete oxide

64 or hydroxide particles (Lafon et al., 2004). According to the classical terminology of soil scientists

65 (Sumner, 1963; Anderson and Jenne, 1970; Angel and Vincent, 1978), the latter kind of iron will

66 be referred to as free-iron and its corresponding oxides and hydroxides as iron-oxides. Ten of 16

67 known iron oxides, hydroxides and oxide-hydroxides are known occur in nature, with goethite,

68 hematite and magnetite being the most abundant as rock-forming minerals; ferrihydrite,

69 maghemite and lepidocrocite being intermediately abundant in many locations; and wüstite,

70 akaganéite, feroxyhyte, and bernalite being the least abundant (Cornell and Schwertmann, 2006;

71 Guo and Barnard, 2013). Dust aerosols from arid and semi-arid regions typically contain goethite,

72 hematite, ferrihydrite and magnetite,   and based on the mass contribution, hematite and goethite

73 are the major components of free-iron in the atmospheric dust aerosols (Schroth et al., 2009; Shi et

74 al., 2012; Takahashi et al., 2013). Hematite (Fe_2O_3) is very common in hot, dry soils and imparts a

75 red color to its sediments. Goethite (α-FeOOH) is a common weathered product in soils and

76 loesses. It occurs in moist, acidic soils (Schwertmann, 1993), and is brown to yellow in color.

77   Sokolik and Toon (1999) found that hematite is an especially strong absorber at ultra-violet

78 (UV) and visible wavelengths, and it can also enhance the absorption of clay minerals and quartz

79 through the formation of aggregates. Derimian et al. (2008) mentioned that iron oxides (primarily

80 hematite and goethite) only affect the optical absorbing ability of aeolian dust at short wavelengths

81 (the blue spectral region). Since the importance of hematite relative to other dust mineral

82 components was discussed more fully in the study of Sokolik and Toon (1999), most subsequent

83 modeling studies have assumed the iron-oxides in dust aerosols to be in the form of hematite. An

84 opposite viewpoint was put forward, however, by Balkanski et al. (2007) who have argued that the

85 optical absorption of dust with hematite at visible wavelengths might be lower than previous

86 thought. The main reason is that internal mixing rule calculations with a hematite content of 1.5

87 volume % (or 2.8 weight %) was supposed to be representative for median dust absorption and

88 was, as well, consistent with the AERONET measurements.

89   However, recent measurements on dust samples from east Asia, northern Africa and western

90 Africa (Lafon et al., 2006; Formenti et al., 2008; Reynolds et al., 2014) indicated that goethite was

91 presented in higher concentration than hematite (i.e. the ratio of goethite to hematite is about 7:3, a

92 result that will be detail introduced in Section 3.2.2). For dust in snow, goethite is also the

93 dominant ferric oxide that detected by reflectance spectroscopy and thus appears to be the main

94   iron-oxide control on absorption of solar radiation (Reynolds et al., 2013). More recently hematite

95   and goethite has been taken into account interactively in global climate simulations due to the

96   availability of global mineralogical distribution maps (Nickovic et al., 2012; Journet et al., 2014).

97   Furthermore, Müller et al. (2009) have measured the spectral imaginary refractive indices of

98   hematite over the wavelengths from 590 nm to 790 nm during laboratory experiments, but these

99   derived values are much lower than the data that employed in Sokolik and Toon (1999). The

100   theoretical simulations of optical scattering of hematite and goethite at 470, 550, and 660 nm by

101   Meland et al. (2011) also found that differences are apparent for hematite in both the phase

102   function and polarization results at 660 nm where the imaginary indices from different references

103   differ. Additionally, two studies that refer to optical properties of hematite in dust samples have

104   also argued that the imaginary values of hematite refractive index in Sokolik and Toon (1999) are

105   more than a factor of 2 larger than those reported by Bedidi and Cervelle (1993) and Longtin et al.

106   (1988) at wavelengths below 600 nm (Moosmüller et al., 2012; Wagner et al., 2012).

107   Thus, what is the real role of iron-oxides in determining the overall impact of the optical

108   properties of dust aerosols? This study will focus on investigating this important scientific

109   question by considering heterogeneous optical refractive indices, mixing states and more logical

110   abundance of iron-oxides.

111

112   **2. Method and simulation**

113   **2.1 Complex refractive index**

114   The complex refractive index (optical constant) is the most basic and significant parameter

115   for calculating the   optical properties of aerosols, but values for the optical constants of hematite

116   in the wavelength range 0.2 to 50 μm are scarce in published references. Table 1 compiles

117   information about the complex refractive indices of the major constituents of free-iron that we

118   have found in the published literature. Sokolik and Toon (1999) employed the refractive indices of

119   hematite from Querry et al. (1978), but Querry et al. (1978) mainly studied the optical constants of

120   limestone and, as far as we can discover, do not contain any work on hematite at all. Since the

121   publication of Sokolik and Toon (1999), studies (Höller et al., 2003; Alfaro et al., 2004; Muñoz et

122   al., 2006; Mishra and Tripathi, 2008; Otto et al., 2009; Meland et al., 2011; Wagner et al., 2012)

123   have misquoted the data as Querry et al. (1978) or Querry (1987) when modeling the optical

properties of hematite. Actually, Querry (1987) is entitled "Optical constants of minerals and other materials from the millimeter to the UV" and gives optical constants of 29 materials, but still without referring to hematite. After careful searching, we have found that Querry (1985) has tabulated values for the refractive index ($m = n + ki$) of hematite. Moreover, Longtin et al. (1988) also reported spectral refractive indices for hematite from earlier measurements by Steyer (1974), Onari et al. (1977), Galuza et al. (1979) and Kerker et al. (1979). This dataset also has been used in modeling the contribution of hematite to the optical properties of atmospheric dust aerosols in recent studies (Klaver et al., 2011a; Köhler et al., 2011; Hansell et al., 2011). Recently, the third unpublished continuous refractive indices of hematite (named TA2005 in Table 1) from the Aerosol Refractive Index Archive (ARIA) of Oxford University have been employed in the Community Atmosphere Model (Scanza et al., 2015). Because this work has not been peer-reviewed and because TA2005 and QE1985 show a similar wavelength dependency we pay special attention to the differences of refractive indices between QE1985 and LG1988 in this paper. Any errors due to uncertainties in the optical constants would be directly reflected in the calculated results referred to above.

Table 1. Summary of the published complex refractive indices for major constituents of free-iron at different wavelengths (with their references).

Iron-oxide species	Wavelength (μm)	Reference source	Abbreviation
Hematite	8.3-50	Popova et al. (1973)	PV1973
Hematite	1.0-333	Onari et al. (1977)	OA1977
Hematite	0.25-0.7	Shettle and Fenn, (1979)	SF1979
Hematite	0.35-0.65	Hsu and Matijevic, (1985)	HM1985
Hematite	0.21-90	Querry (1985)	QE1985
Hematite	0.3-300	Longtin et al. (1988)	LG1988
Hematite	0.2-0.7	Gillespie and Lindberg, (1992)	GL1992
Hematite	0.2-4.5	Krekov (1992)	KE1992
Hematite	0.35-0.75	Bedidi and Cerville (1993)	BC1993
Hematite	0.1-1000	Triaud (2005)*	TA2005
Hematite	5-50	Marra et al. (2005)	MR2005
Hematite	5-2000	Glotch and Rossman, (2009)	GR2009
Hematite	0.59-0.79	Müller et al. (2009)	ML2009
Magnetite	0.21-55	Querry (1985)	QE1985
Magnetite	5-50	Mukai (1989)	MK1989
Magnetite	0.25-0.7	Gillespie and Lindberg, (1992)	GL1992
Magnetite	0.1-1000	Amaury et al. (2002)	AU2002
Magnetite	5-100	Glotch and Rossman, (2009)	GR2009

|			
Goethite	0.45-0.75	Bedidi and Cerville, (1993)	BC1993
Goethite	8-50	Glotch and Roman, (2009)	GR2009
Wüstite	0.2-500	Henning (1995)	HN1995
Wüstite	10-500	Henning and Mutschke, (1997)	HN1997

142   * The data was taken from http://www.atm.ox.ac.uk/project/RI/hematite.html

143   Bedidi and Cervelle (1993) also presented refractive indices for hematite and goethite

144   derived from reflectance measurements at wavelengths of 350-750 nm. Glotch and Rogers (2007)

145   reported the optical constants of hematite, goethite and magnetite over the infrared (IR)

146   wavelengths, and Hsu and Matijević (1985) also measured the refractive indices of hematite in the

147   wavelengths of 350-650 nm.

148   Hematite is a uniaxial crystal which crystallizes in the trigonal system, whose optic axis

149   corresponds to the crystallographic *c*-axis. Perpendicular to the *c*-axis are two radial *a*-axes. The

150   dielectric constants of bulk hematite must therefore be measured for two principal polarizations of

151   the incident light, namely one with the electric vector in any direction perpendicular to the *c*-axis

152   (the so-called ordinary ray or − O ray) and the other with the electric vector along the crystalline

153   *c*-axis (the extraordinary ray or − E ray). In this work we have calculated the average refractive

154   indices for anisotropic hematite from all references in Table 1. The formula used is adopted from

155   Longtin et al. (1988) and is:

156   $$m_{avg} = (2n_{E-ray} / 3 + n_{0-ray} / 3) + (2k_{E-ray} / 3 + k_{0-ray} / 3)i.$$

157   The reported values for the complex refractive index from the sources in Table 1 are

158   markedly different, especially the imaginary part which controls the optical absorption. In order to

159   visually demonstrate the variation of optical constants from different references, values of the real

160   (n) and logarithmic values of imaginary parts (k) are shown in Figure 1.
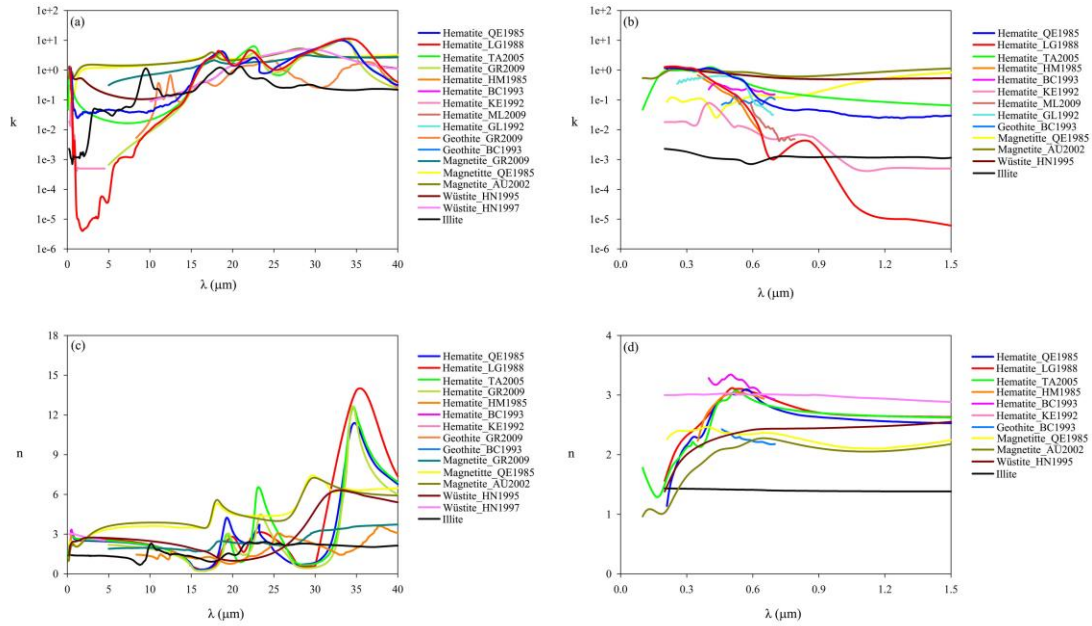
Fig. 1. Spectral distribution of the imaginary and real parts of the complex refractive index for different iron oxides from Table 1 at wavelengths of 0 to 40 μm (Panels (a) and (c)) and expanded for wavelengths of 0 to 1.5 μm (Panels (b) and (d)).

For the real part of the refractive index for iron-oxides, there is a reasonable agreement between the hematite and magnetite datasets from the different references (Figure 1c). Because the real refractive index of hematite shows large fluctuations at wavelengths longer than 18 μm due to anisotropic refraction, the agreement between the different datasets decreases at these wavelengths. For goethite we are aware of only two sets of optical constants: one at visible wavelengths from Bedidi and Cervelle (1993) and the other at IR wavelengths from Glotch and Rogers (2007), but the wavelength gap between these two datasets hampers continuity. Unfortunately, Meland et al. (2011) have checked the former dataset for goethite using simulations according to Mie and T-Matrix theories and show that it may be in error. Nevertheless, we can see that goethite has optical constants similar to hematite. The real refractive index of hematite is larger than that of magnetite at wavelengths less than 2μm, but is smaller between 2 and33 μm (Figures 1c&d).

For the imaginary part of the refractive index of iron-oxides, hematite and goethite have different optical properties at short wavelengths, both in terms of magnitude and spectral dependence (Bedidi and Cervelle, 1993). Between 460 and 700 nm the imaginary part of the complex refractive index (representing absorption) of goethite is up to 3 times smaller than that of hematite. As a consequence, the proportions of hematite and goethite in mineral dust can

182 potentially change the magnitude and the spectral dependence of shortwave absorption of mineral

183 dust. However, the limited and discontinuous refractive indices of goethite have constrained the

184 evaluation of the effects of specific compositions of goethite and hematite to dust optical

185 properties and solar radiation balance over broader wavelength ranges.

186 From Figure 1a, we clearly see that the k values for hematite from QE1985 and from

187 LG1988 show significant differences for wavelengths between 650 nm and 15 μm. These

188 differences are present at visible wavelengths and disappear at ultraviolet wavelengths, but the two

189 datasets have similar trends at UV and visible wavelengths (Figure 1b). Note that the hematite

190 optical constants vary dramatically across the visible wavelengths. In particular, the imaginary

191 part of the index for hematite shows a sharp decrease with increasing wavelength in the red. As a

192 consequence there is a large variability in the imaginary refractive index values for hematite taken

193 from different published references, particularly at 2 μm where the values from different sources

194 differ by a factor of 8600. Thus, this study firstly focuses on what will be the result if these

195 heterogeneous optical constants of hematite are used as input for the calculation of radiation

196 transfer models.

197

198 **2.2 Particle size distribution**

199 Size distribution is another important factor that affects the optical properties of particles.

200 Because Sokolik and Toon (1999) has employed the refractive index dataset for hematite from

201 QE1985 to calculate the radiative properties, we adopt here the same particle size distribution but

202 with the refractive index dataset for hematite from LG1988 to compare our results with Sokolik

203 and Toon (1999). The lognormal distribution is applied to dust aerosols:

204 $$n_n(\ln r) \equiv \frac{dN}{d\ln r} = \frac{N_0}{\sqrt{2\pi}\ln\sigma}\exp\left[-\frac{1}{2}\left(\frac{\ln r - \ln r_0}{\ln\sigma}\right)^2\right],$$

205 where r_0 is the median radius, σ is the geometric standard deviation, and N_0 is the total

206 particle number density of the component in particles per cubic centimeter.

207 The optical properties of minerals are calculated on the assumption that they have one size

208 mode but varying median radius. The particle size modes are selected as $r_0 = 0.5$ and 0.7 μm, and

209 $\sigma = 2.0$. The size mode with median radius $r_0 = 0.5$ μm is believed to be representative of the

210   particle size distribution of the long-lived, long-distance-transport mode of airborne dust

211   (Patterson and Gillette, 1977; Arimoto et al., 1997). The larger r_0 is representative of a particle

212   size mode which occurs near the dust source (Gomes and Gillette, 1993). In reality, the size

213   distribution of dust aerosols can have one or several modes, characterized by a specific

214   composition (Mahowald et al., 2013).

215

216   **2.3 Theoretical simulations**

217   Images from scanning electron microscopy (SEM) reveal non-spherical, irregular and

218   compact shapes of the dust particles (Figure 3), but Otto et al. (2009) and Klaver et al. (2011b)

219   have shown that spherical/non-spherical differences only influence the single scattering albedo by

220   less than 1%. Meland et al. (2011) have also shown that moderate departures from spherical shape

221   are relatively unimportant in determining the scattering matrix for particles with high refractive

222   index values, such as hematite. Therefore, we expect the aerosol asphericity to have a negligible

223   impact on our calculated results of optical properties and subsequent calculations using the Mie

224   theory (which assumes a spherical morphology for the dust particles).

225   There are several different computer codes that can be used to compute optical properties

226   for a lognormal particle size distribution. The theoretical light scattering simulations in this paper

227   have used the MieTab software. MieTab uses a FORTRAN code with continued fraction

228   modification produced by W. J. Lentz from the Mie code originally developed by Dave and Center

229   (1968). This modified code can be obtained from

230   http://diogenes.iwt.uni-bremen.de/vt/laser/codes/ddave.zip. In order to validate the accuracy of

231   MieTab, we firstly compared it with a double precision Lorenz-Mie scattering code and a double

232   precision T-Matrix code for a lognormal particle size distribution from Mishchenko et al. (2002).

233   The double precision Lorenz-Mie and T-Matrix codes are available from

234   http://www.giss.nasa.gov/staff/mmishchenko/t_matrix.html.

235   In addition to the wavelength dependent optical constants and the size distribution, the

236   T-Matrix theory also requires assumptions about the particle shape. In this work we use an aspect

237   ratio of 1.000001 to represent a spherical particle shape, because use of an aspect ratio exactly

238   equal to 1 causes computational overflow in some cases. The calculated results from the three

239   codes at different wavelengths and complex refractive indices for the same size distribution are

240   listed in Table 2. The good agreement of the results from the three codes demonstrates that the

241   possibility of computational error affecting the interpretation of the calculated optical properties of

242   iron-oxides can be neglected.

243

244   **Table 2.** Comparison of simulated optical properties between MieTab, Lorenz-Mie and T-matrix methods.

Wavelength	550 nm			633 nm			1060 nm		
$m=n+ki$	n=3.102, k=0.0925			n=3.007, k=0.00974			n=2.66, k=0.00003		
Code type	MieTab	T-matrix	Lorenz-Mie	MieTab	T-matrix	Lorenz-Mie	MieTab	T-matrix	Lorenz-Mie
Q_{ext}	2.0950	2.1332	2.1637	2.1440	2.1917	2.2585	2.3250	2.5042	2.0226
Q_{sca}	1.2640	1.3284	1.3233	1.8500	1.9048	1.9587	2.3240	2.5033	2.0216
Q_{abs}	0.8310	0.8048	0.8404	0.2940	0.2870	0.2998	0.0010	0.0009	0.0010
ω_0	0.6033	0.6227	0.6116	0.8629	0.8691	0.8673	0.9996	0.9996	0.9995

245

246   **3. Results and discussion**

247   **3.1 Basic optical properties**

248   We focus here on modeling the spectral optical properties of iron-oxides which are needed

249   for climate modeling: the volume extinction coefficient β_{ext} (which is the sum of the scattering

250   coefficient β_{sca} and the absorption coefficient β_{abs}), the single scattering albedo ω_0, and the

251   asymmetry parameter g (a cosine weighted integral of the scattering phase function). This set of

252   parameters allows the calculation of radiation forcing in most climate models. Figure 2 shows

253   calculated optical parameters for hematite (with complex refractive indices from QE1985 and

254   LG1988) and illite with varying median radius at solar and infrared wavelengths. The volume total

255   extinction coefficients β_{ext} have been normalized as β_{ext}^* for particle number concentration $N=1$

256   cm^{-3}.
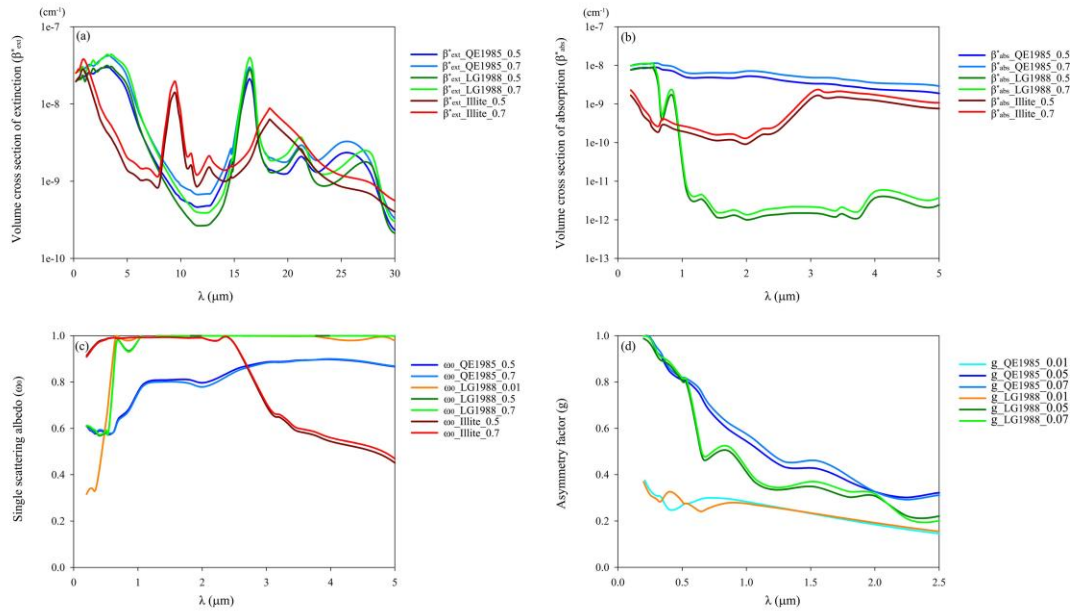
Fig. 2. The calculated spectral optical properties for hematite, goethite and illite with different complex refractive index and size distribution. (a) Volume cross section of extinction, (b) Volume cross section of absorption, (c) Single scattering albedo and (d) Asymmetry factor

Figure 2a and Figure 2b demonstrate how the normalized spectral extinction coefficient and the normalized spectral absorption coefficient vary due to the differences in the refractive indices and median radius of the minerals. As shown in Figure 2a, β^*_{ext} for hematite has a spectrum which is clearly distinguishable from that for illite at UV, visible and IR wavelengths. One point should be noted: hematite has a lower normalized spectral extinction coefficient than illite at wavelengths less than 1.3 μm, which means that hematite has a weaker optical extinction capacity than illite at these wavelengths. In the IR region, the spectral features of hematite in β^*_{ext} show large differences in volatility, and mimic the features in the refractive index of hematite. The magnitude of β^*_{ext} depends on the parameters of the particle size distribution.

Figure 2b shows the equivalent normalized spectral absorption coefficient for hematite from QE1985 and LG1988 at wavelengths less than 5 μm. The normalized absorption coefficient of hematite from QE1985 is about 100 times larger than that for illite at both visible and near-IR wavelengths, but the normalized absorption coefficient for hematite from LG1988 has larger values than those for illite at wavelengths less than 1 μm and about 100 times smaller values than

those for illite at wavelengths between 1 μm and 5 μm. If we adopt the complex refractive indices of QE1985, the calculated absorption coefficient of hematite indicates that hematite is an especially strong absorber at UV and visible wavelengths. Conversely, the calculated absorption coefficient of hematite using LG1988 data suggests that hematite is an important aerosol component only for short-wavelength absorption. Considering the whole region from 0.2 μm to 5 μm, hematite with complex refractive indices from LG1988 has an approximately equal absorbing capacity to that of illite.

Figure 2c illustrates the single scattering albedo of hematite and illite at wavelengths between 0.2 μm and 5 μm for different particle size distributions. The single scattering albedo of hematite is about 0.6 for wavelengths $\lambda < 0.55$ μm and varies little from $r_0 = 0.7$ μm to $r_0 = 0.5$ μm. In contrast, illite has ω_0 in the range from about 0.9 to 1 for $\lambda < 0.55$ μm, showing strong spectral dependence at short wavelengths. For $\lambda > 0.55$ μm, illite has ω_0 of about 0.99 for $0.55 < \lambda < 2.0$ μm and this gradually reduces to about 0.5 for $2.0 < \lambda < 5.0$ μm, while hematite shows large differences of ω_0 depending on the source of the refractive indices. The single scattering albedo decreases to about 0.35 at UV wavelengths for hematite nanoparticles (which are always observed as aggregates with other clay mineral particles) with $r_0 = 0.01$ μm and $\sigma = 2.0$, but it rapidly increases to nearly 1 at wavelengths $\lambda > 0.7$ μm.

Figure 2d compares the asymmetry parameter of hematite with refractive indices from QE1985 and LG1988 at UV and visible wavelengths with size modes of $r_0 = 0.7$, 0.5, and 0.01 μm. For $r_0 = 0.5$ and 0.7 μm, hematite from QE1985 has $g = 0.3$ - 0.99, g decreasing as λ increases. The magnitudes of g from LG1988 are in the range from 0.2 to 0.99 with a few fluctuations. For $r_0 = 0.01$ μm, both datasets put g in the range from about 0.15 to 0.38. Thus, the magnitude of g depends significantly on the particle size distribution.

**3.2 Physical and mineralogical properties**

3.2.1 Size and Morphology

Many electron microscopy observations (Greeland et al., 1968; Tipping, 1981; Postma and Brockenhuus-Schack, 1987; Poulton and Canfield, 2005; Raiswell and Anderson, 2005; Shi et al., 2009; Deboudt et al., 2012; Wagner et al., 2012; Guo and Barnard, 2013) have shown that poorly

305   ordered iron-oxides commonly occur as spheroidal to ellipsoidal nanoparticles that may be single

306   or aggregated, and may be unattached or attached to quartz or clay minerals (Figure 3). The

307   reasons for the aggregation and the attachment are not well understood but are likely to be related

308   to interactions of surface charge characteristics between iron-oxides and quartz or clay minerals

309   (Poulton and Canfield, 2005). According to Hinds (1982), the binding mechanisms that hold

310   separate aerosols together in an agglomerate formed in the air include the van der Waals force, the

311   electrostatic force and the surface tension of adsorbed liquid films. As mentioned above, the

312   dispersed nanoparticles of iron-oxides which are attracted to larger dust particles have more

313   prominent optical absorption than aggregated iron-oxides, but the use of size distributions for

314   nanoparticles (such as $r_0 = 0.01$ μm and $\sigma = 2.0$) will overestimate the optical absorption of

315   iron-oxides in natural dust aerosol samples.

316
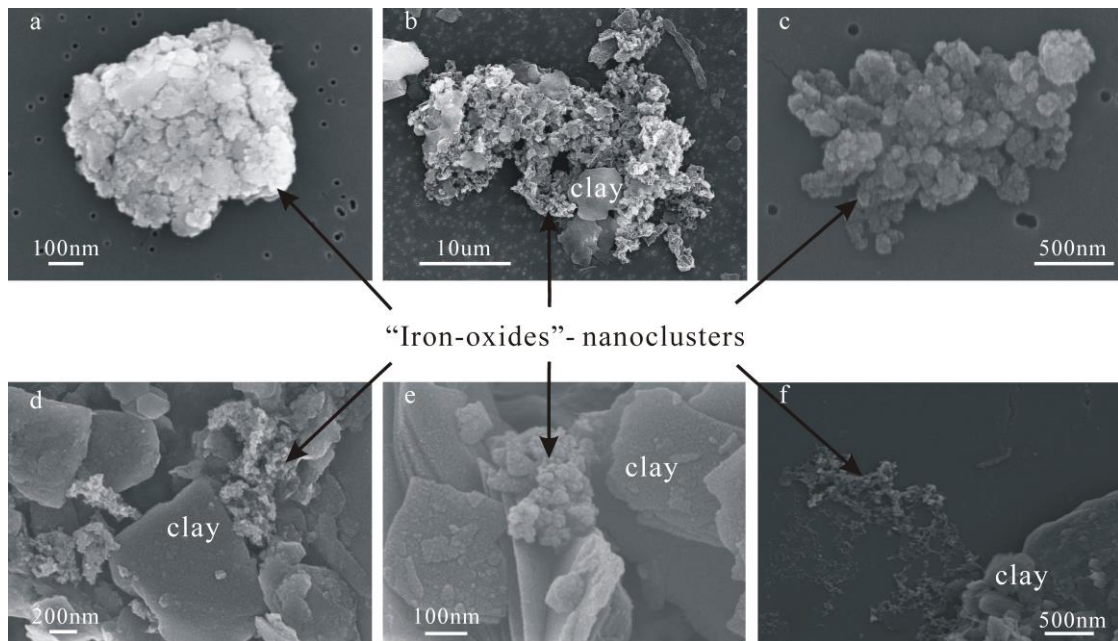
318   **Fig. 3.** Representative morphology of iron-oxide aggregates in dust samples observed by SEM.

319

320   **3.2.2 Abundance of total iron and iron-oxides**

321   By employing the optical parameters of hematite and clay minerals calculated above, we can

322   model the optical effects of hematite in dust aerosols. Problems associated with this are the actual

323   variation of iron-oxides content and the state of the mixture with other minerals and these should

324   be accounted for when modeling the optical properties of dust aerosols.

325   The total iron content in dust aerosol bulk samples is always measured in terms of the Fe_2O_3

326 mass percentage of the total oxide mass by elemental analysis (i.e. XRF, PIXE or ICP). Ganor and

327 Foner (1996) gave a median Fe content of 2.9% for dust storms in Israel. The observed Fe

328 percentage for the Dunhuang site in China during ACE-Asia is 4.0 ±0.9% (Zhang et al., 2003). A

329 value of 4.45 ±0.49% (Guieu et al., 2002) has been proposed as characterizing Saharan dust. The

330 elemental analysis by XRF yielded total iron oxide contents between 2.0 and 5.0 weight % for

331 four Saharan mineral dust samples of different color and origin (Linke et al., 2006). Moreover,

332 Lafon et al. (2004) and Lafon et al. (2006) reported that the total iron content (the Fe_2O_3

333 percentage) varies from 6.2% to 8.7% in six atmospheric samples and three wind tunnel generated

334 samples. The total iron content ranges from 1.82% to 11.8% (with an especially high value of 30.0%

335 in the sample collected from Bamako, Mali) in entrained $PM_{2.5}$ from ten soil samples representing

336 the Arabian Peninsula, the Sahara and Sahel regions and samples from northeast Africa and

337 south-central Asia (Moosmüller et al., 2012). Furthermore, percentage values of iron content from

338 several datasets reported by previous studies vary mainly between 4 and 11% (e.g., Gomes and

339 Gillette, 1993; Chiapello et al., 1997; Gao et al., 2001; Journet et al., 2014).

340 One additional aspect should be discussed here for the proper interpretation of the obtained

341 data: how representative is the total iron concentration of the free iron oxide content of dust

342 aerosols? Free-iron is present as a major aerosol component affecting the short-wavelength

343 absorption of mineral dust. However, iron oxide represents only part of the total iron, which may

344 also exist in the crystal lattice of numerous other dust minerals. The iron oxide-to-total iron ratio

345 in natural and soil-derived aerosols has been characterized by applying an adapted reductive

346 extraction method as commonly used in soil science (Lafon et al., 2004; Lafon et al., 2006). This

347 method provides no structural information about the extractable iron and therefore cannot

348 distinguish between the presence of goethite or hematite in the samples. Fortunately，this method

349 can provide an upper limited to the free-iron content for the optical modeling.

350 Lafon et al. (2004) and Lafon et al. (2006) reported considerable variability in the iron

351 oxide-to-total iron ratio for various regions and sampling conditions and that there is no clear

352 relationship between the oxide-to-total iron ratio and dust origin or aging. Based on all the values

353 for the oxide-to-total iron ratio reported in the published literature (Lafon et al., 2004; Lafon et al.,

354 2006; Alfaro et al., 2004; Formenti et al., 2008; Klaver et al., 2011a), we have calculated an

355 average of 0.52. Formenti et al. (2014a) reported that iron oxides account, by mass, for 0.38 to

0.72 of the total elemental iron based on X-ray absorption analysis of samples of mineral dust emitted from or transported to western Africa. Reynolds et al. (2013) reported that the percent iron in goethite and hematite relative to iron in all iron-bearing phases ranges from 0.2 to 0.52 for dust samples in Australia as determined from Mössbauer spectra. Based on an average compiled from the literature, Kandler et al. (2009) and Kandler et al. (2011) have assumed that only 20% of the total iron content is hematite when determining the complex refractive index of dust aerosols. Alfaro et al. (2004) found in their dust samples comparable total iron contents in the range of 3.0 to 6.5 weight %, and they assigned a significant amount of 2.8 to 5.8 % of this iron as present in iron oxide mineral phases. This result is consistent with the reported 2.8 - 5.0% of free-iron in aerosol samples collected from three different locations over the world (Lafon et al., 2004; Lafon et al., 2006). Takahashi et al. (2011) indicated that the content of iron-oxides is less than 5 weight % in Asian dust. Moreover, Klaver et al. (2011a) reported that the iron oxides-to-total iron ratio for the analysed samples varied between 0.4 and 0.61, accounting for between 1% and 3% of the total gravimetric mass, and Formenti et al. (2008) also illustrated that iron oxides (speciation hematite and goethite) represented 2.4% and 4.5% of the total mineral dust mass. As mentioned above, only about half of the total iron content is represented by free-iron.

XRD analytical technology has also been applied to identify the content of hematite and goethite in some cases and less than 2% iron oxides was detected (Shi et al., 2005; Linke et al., 2006b; Kandler et al., 2009; Lawrence et al., 2010; Klaver et al., 2011a; Wagner et al., 2012; Formenti et al., 2014b). Depending on the crystal phase of interest, this method has a detection limit of 0.1 to 0.5 weight % for iron oxides (Balsam et al., 2014). Discrepancies between the quantified free-iron content detected by the method of Lafon et al. (2006) and the hematite or goethite contents determined by XRD could be due to difficulties of the Rietveld method associated with poor crystallographic ordering of iron oxides in mineral dusts.

Single particle analysis has also been conducted for detecting the free iron oxides. Fe-rich particles (iron oxides) represented no more than 5% of the particle number in aerosol samples and hematite or goethite were found more often in the fine fraction(Chou et al., 2008; Kandler et al., 2009; Schladitz et al., 2009; Kang et al., 2009; Scheuvens et al., 2011; Malek et al., 2011; Wagner et al., 2012; Menéndez et al., 2014).

Table 3. Summary of global reported ratios of hematite to goethite (Hm/Gt) in dust aerosols.

Location (Number of samples)	Type	Method	Average value of Hm/Gt	Reference
Niger (1)	Aerosol*	DRS	0.5625	Lafon et al. (2006)
Tunisia (1)	Aerosol*	DRS	0.4085	Lafon et al. (2006)
China-Zhenbeitai (1)	Aerosol	DRS	0.3514	Lafon et al. (2006)
Niger (99)	Aerosol	DRS	0.4286	Formenti et al. (2008)
Niger (12)	Aerosol	XAS	0.5771	Formenti et al. (2014a)
Gran Canaria (19)	Aerosol	DRS	0.9048	Lázaro et al. (2008)
North Atlantic (9)	Aerosol	DRS	0.9276	Arimoto et al. (2002)
Muztagata (7)	Aerosol	DRS	0.6918	Xu et al. (2014)[+]
Golmod (29)	Aerosol	DRS	0.7262	Yang et al., (2014)
Tazhong (6)	Aerosol	DRS	0.9157	Lu et al. (2011)
Dunhuang (29)	Aerosol	DRS	0.8762	Shen et al. (2006)
Yulin (32)	Aerosol	DRS	0.7158	Shen et al. (2006)
Horqin (22)	Aerosol	DRS	0.7448	Shen et al. (2006)
Australia (6)	Aerosol	MS	0.4571	Reynolds et al. (2014)

* Dust aerosol produced by wind tunnel; [+] Unpublished paper of the fourth author, private communication.

The technology of diffuse reflectance spectroscopy (DRS) has normally been to quantify the ratio of hematite to goethite in a particular dust sample (Lafon et al., 2006; Shen et al., 2006; Lázaro et al., 2008; Formenti et al., 2008; Formenti et al., 2014a). The accurate quantification of goethite and ferrihydrite in dust is extremely difficult owing to similarities in structure and associated absorption spectra of these two minerals (Scheinost et al., 1998; Torrent and Barrón, 2002; Schroth et al., 2009). This has the critical implication that the content of goethite measured by absorption spectroscopy is actually the sum of goethite and ferrihydrite. This does not, however, affect the optical calculations due to their optical similarity. Table 3 summarizes the measured ratios of hematite to goethite in global dust aerosol samples and shows higher ratios of Hm/Gt in Asian dust samples compared to African samples. Over the whole world, it is concluded that goethite predominates over hematite with a relative abundance of 50% - 75% of iron oxides in dust aerosols.

Based on the above reported results, we conclude that the iron-oxides account for approximately half of the mass of elemental Fe and for between 2 and 5 % of the dust mass. Most

401   of them are composed of goethite, representing between 50 and 75 % of the iron oxide mass.

402

403   **3.2.3 Mixing states**

404   As free-iron particles are always mixed with other kinds of particle, the condition of the

405   mixture could be important for their ability to scatter and absorb radiation. The 3D structure of

406   iron-oxide particles obtained by tomography reveals that these Fe-rich inclusions are often found

407   at the surface of aluminosilicate particles but that some are also included inside particles (Deboudt

408   et al., 2012). Inversions calculated assuming external mixing are better able to explain the

409   wavelength dependence of dust absorption by varying only hematite concentration than inversions

410   using internal mixing (Koven and Fung, 2006; Formenti et al., 2014a). Thus, a semi-external

411   mixing assumption is clearly an optimal approximation for iron-oxides mixed with aluminosilicate

412   particles. Moreover, this assumption has the advantages of simplicity of calculation, interpretation,

413   and the possibility of comparing with model results.

414

415   **3.3 Further simulation and verification**

416   Sokolik and Toon (1999) also suggested that the radiative properties of a mixture would

417   strongly depend on the relative abundance of individual minerals due to the large variations in the

418   optical properties of individual minerals. Therefore, we model the optical properties for a range of

419   possible weight fractions of hematite in the clay-size mode while the remaining mass is illite

420   which represents the clay minerals. As mentioned above, we adopt 0% hematite as the lower limit

421   for the aerosol samples with no free-iron particles, 2.5% hematite for the transported dust aerosol

422   samples, 5% hematite for the locally emitted dust samples and 7.5% hematite for the upper limit.

423   Due to the limited and discontinuous refractive indices of goethite, this setting may underestimate

424   the actual optical effects of goethite in dust aerosol. Using the density of hematite (5.3 g/cm^3) and

425   illite (2.75 g/cm^3), volumetric hematite fraction was converted from the mass hematite fraction to

426   calculate the effective complex refractive indices for dust.

427   Dust mineralogical composition is often expressed as a weighted fraction of individual

428   components in the total dust sample. Because the relationship of number concentration and mass

429   concentration can be expressed as:

430
$$M_i = M_0 \cdot W_i = N_i \cdot \rho_i \cdot \frac{4}{3} \pi(r_0)^3 \cdot \exp\left[\frac{9}{2}(\ln \sigma)^2\right],$$

431 where M_i, N_i, W_i and ρ_i are the particle mass concentration, number concentration, weight

432 fraction and density of the i-th mineral in the mixture respectively and M_0 is the total particle

433 mass concentration of the mixture sample, the optical properties of external mixtures of minerals

434 can be modeled by:

435
$$K_{ext}^{mix} = \sum (K_{ext(i)}^* \cdot N_i) = \sum \left(K_{ext(i)}^* \cdot \frac{M_0 \cdot W_i}{\rho_i \cdot \frac{4}{3}\pi(r_0)^3 \cdot \exp\left[\frac{9}{2}(\ln \sigma)^2\right]}\right)$$

436   Figure 4a shows the differences between the single scattering albedo calculated for the

437 mixture of illite and hematite with complex refractive indices from LG1988 at visible and infrared

438 wavelengths. Compared to ω_0 for illite with no hematite, it is not hard to see that ω_0 for mixtures

439 with different amount of hematite show significant differences in four wavelengh ranges, namely,

440 0.2 - 0.7 μm, 2.5 - 8.7 μm, 8.7 - 12.5 μm and 15.0 - 17.5 μm. For $0.2 < \lambda < 0.7$ μm and $15.0 < \lambda <$

441 17.5 μm, ω_0 for the mixtures is smaller than ω_0 for pure illite, which means the presence of

442 hematite enhances the optical absorption of the mixtures. For $2.5 < \lambda < 8.7$ μm, ω_0 for the

443 mixtures is larger than for pure illite, which means the presence of hematite enhances the optical

444 scattering of the mixtures. But for $8.7 < \lambda < 12.5$ μm, ω_0 shows more complicated fluctuations.

445
446
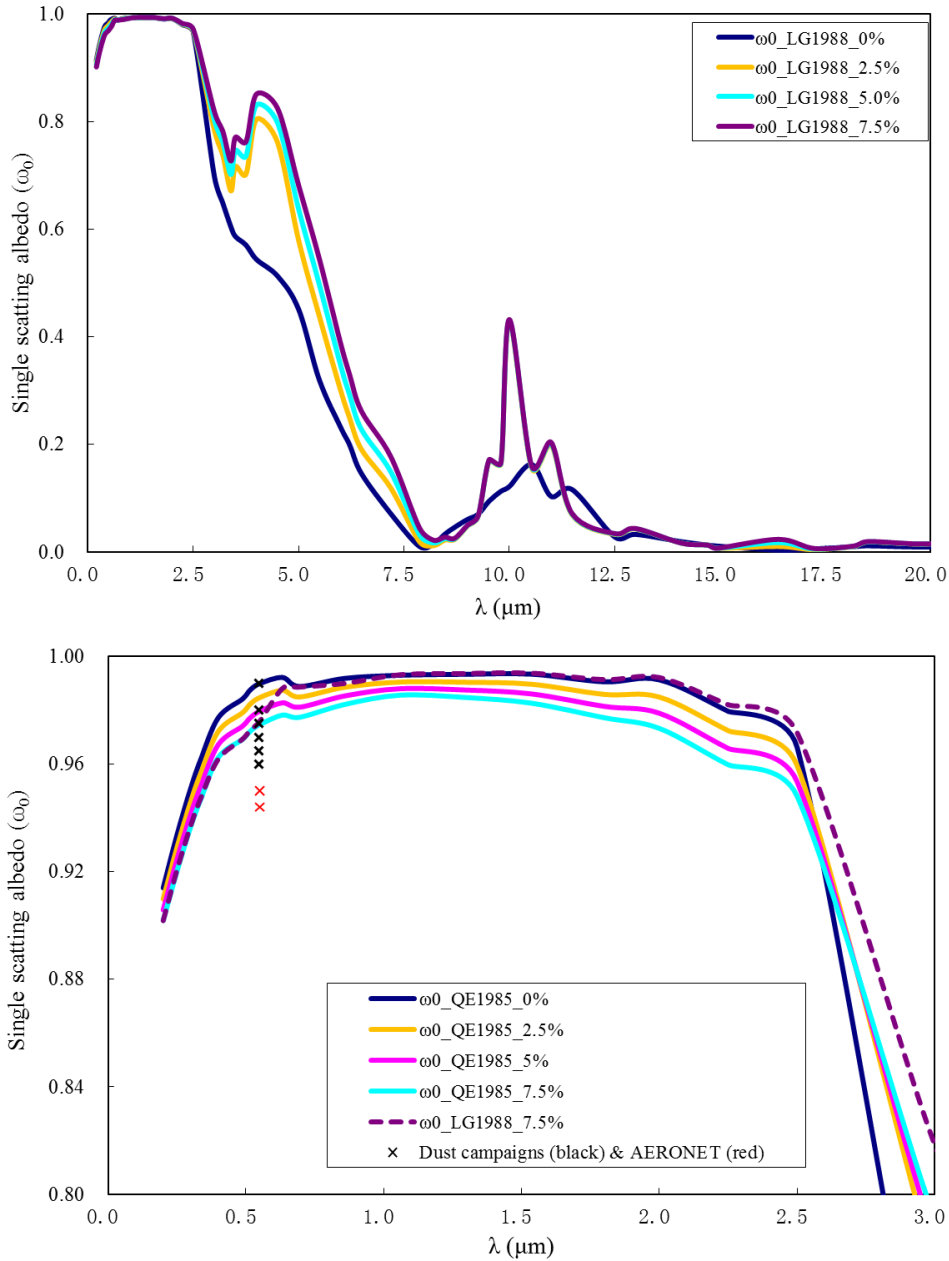
Fig. 4. Spectral single scatting albedo (SSA) for mixtures of illite and hematite with varying percentages and refractive indices at wavelengths of 0-20 μm (a) and 0-3 μm (b) with comparison to field observed results at 550nm.

Figure 4b shows the differences between ω_0 for illite mixed with different amounts of hematite with refractive indices from QE1985 at solar wavelengths. The magnitude of ω_0 for a mixture increases when the median radius r_0 increases. In order to compare the effects for hematite with refractive indices from two different sources for the same mixture state, we also plot ω_0 for illite mixed with 7.5% hematite with refractive indices from LG1988 in Figure 4b.

457   Evidently, for $0.55 < \lambda < 2.5$ μm, the dataset of QE1985 will lead to higher optical absorption,

458   although the two datasets have the same optical scattering and absorption for $\lambda < 0.55$ μm.

459   Another question is what is the competition between theoretical calculated values and field

460   observed results? In order to compare our calculated SSAs with measured values, we review all

461   reported SSAs during different dust campaigns or inferred from AERONET measurements, and

462   listed them in Table 4. The measured results for dust mixed with BC were excluded during our

463   review progress, such as the results from the campaign of AMMA. The measurements from

464   DABEX are comparable but on the lower edge of previous measurements performed at 550 nm

465   during the TARFOX, SHADE, GERBILS, SAMUM, NAMMA and Fennec 2011 field campaigns.

466   Absorption from the mineral dust as measured using the corrected nephelometer and Particle Soot

467   Absorption Photometer (PSAP) combination suggests that single scattering albedos at 550 nm

468   (SSA550) range from 0.91 to 0.97 (with a mean of 0.97) for iron oxide mass fractions between 1.3

469   and 3.5% (Klaver et al., 2011a). The SSAs at 532 nm were reported as 0.99 ± 0.001 and $0.98 \pm$

470   0.002 for the Cairo 2 and Morocco dust samples with Fe_2O_3 mass fractions of 4.5 and 3.63%,

471   respectively (Linke et al., 2006). Johnson and Osborne (2011) revealed that the use of the mineral

472   dust refractive indices from Balkanski et al. (2007) assuming 1.5% hematite gave reasonable

473   agreement with the measured single scattering albedo, consistent with the findings of Klaver et al.

474   (2011a). Haywood et al. (2011) shown that mineral dust is relatively non-absorbing at 550 nm due

475   to the relatively small fraction of iron oxides present (1−3%). Balkanski et al. (2007) addressed

476   this difference and argued that dust absorption at visible wavelengths might be lower than

477   previously thought because mixing rule calculations with hematite content of 1.5% by volume,

478   supposedly representative of median dust absorption, showed a very good agreement with the

479   AERONET measurements. The same question is presented in Figure 7a of Formenti et al. (2014a):

480   that the calculated SSA using a higher imaginary index of iron-oxides also overestimated the

481   absorbing ability of Saharan dust in comparison with field observation.

482   We compare our calculated SSA curves with the measured values in Figure 4b. It is shown

483   that the observed SSAs were mostly ranged in 0.94-0.99 during different dust campaigns, but

484   much lower (0.944-0.95) for the AERONET which cannot exclude the presence of black carbon

485   with higher absorbing. Our calculated result could consistent with the higher part (0.97-0.99) of

486   measured SSAs, but higher than the lower part (0.95-0.97) due to the effect of coarse particles

487   during different dust campaigns. Thus, the iron oxide content alone cannot explain the variability

488   of the single scattering albedo. This suggests that more complete knowledge of the dust

489   mineralogical composition and size distribution with varied multi-modes is needed as input to

490   more rigorous modeling.

491   **Table 4.** Review of measured dust single scattering albedos during dust campaigns and AERONET observations.

References	SSA_550nm (Mean)	S.D.	Observations
Haywood et al. (2001)	0.97	0.02	TARFOX
Haywood et al. (2003)	0.97	0.02	SHADE
Johnson and Osborne (2011)	0.97	0.02	GERBILS
Müller et al. (2011)	0.96	0.03	SAMUM_2
Petzold et al. (2011)	0.975	0.15	SAMUM
Jeong et al. (2008)	0.96	0.01	NAMMA
Osborne et al. (2008)	0.99	0.02	DABEX
Ryder et al. (2013)	0.965	0.015	Fennec 2011
Lack et al. (2009)	0.95	0.01	TexAQS/GoMACCS
Linke et al. (2006)	0.985	0.006	Laboratory
Zhu et al. (2007)	0.95	0.01	AERONET
Kim et al. (2011)	0.944	0.005	AERONET

492

493   In order to check the further effects of the mixing state of hematite on the single scattering

494   albedo, we use two sets of assumptions that bracket the actual state of hematite mixing: internal

495   mixing (Int), in which individual dust particles are a combination of all components present; and

496   external mixing (Ext), in which different components exist as separate particles.

497   For the case of an external mixture of particles, the average optical properties are calculated

498   by summing over the optical properties of the individual species. Approximations have to be made

499   to calculate the optical properties of internal mixed particles. Three common approximations for

500   the calculation of these latter optical properties are the volume mixing method, the Bruggeman

501   approximation and the Maxwell-Garnett approximation (Chýlek et al., 1988; Bohren and

502   Huffman, 1998). Detail information about the three methods is given by Sokolik and Toon (1999).

503   We have calculated the single scattering albedo (SSA) of illite-hematite mixtures with different

504   hematite contents using internal mixing according to the above three internal approximations and

505   also using external mixing.

506   The calculated SSA values for illite-hematite mixtures using internal and external mixture

507   assumptions as a function of wavelength and hematite mass fraction are illustrated in Figure 5. For

508   the case of external mixing, the SSAs at 405 nm show good agreement for refractive indices from

509   QE1985 and LG1988, but the calculated SSAs at 870 nm for hematite with refractive indices from

510   QE1985 are much smaller than those using LG1988. This is explained by Figure 4b where the two

511   datasets have the same optical scattering and absorbing properties for $\lambda < 0.55$ μm but the dataset

512   of QE1985 leads to higher optical absorption for $\lambda > 0.55$ μm. The calculated SSAs with the three

513   different internal mixing methods are all much smaller than those for external mixing both at 405

514   nm and 870 nm since the assumption of an external mixture results in less absorption and less

515   wavelength dependence of absorption than does the assumption of an internal mixture for small

516   amounts of hematite. The basic reason for this is due to the extremely high imaginary refractive

517   index for hematite at short wavelengths. For the case of internal mixing, the SSAs from the

518   volume mixing method are smaller than for the other methods. This is due to the averaged

519   imaginary refractive index being larger than for the other two approximations. On the basis of the

520   study of Peterson (1968), only the effective refractive index of the non-metallic part of the dust

521   can be calculated using the volume mixing method. Thus, adopting the volume mixing method to

522   calculate the optical properties of aerosol samples will lead to a smaller SSA (Levoni et al., 1997;

523   Sokolik and Toon, 1999; Shi et al., 2005; Höller et al., 2003; Ebert et al., 2004; Kandler et al.,

524   2007; Kandler et al., 2009; Petzold et al., 2009; Otto et al., 2009; Wagner et al., 2012).

525   The calculated SSAs using the Bruggeman approximation are consistent with those from the

526   Maxwell-Garnet approximation for low hematite contents at both 405 nm and 870 nm but differ

527   from them for hematite content larger than 10%. Both the Maxwell-Garnet and Bruggeman

528   approximations are derived from the same integral equation for the propagation of electromagnetic

529   waves in an inhomogeneous medium but under a different set of approximations (Chyýlek et al.,

530   1988; Bohren and Huffman, 1998). In previous studies, the Bruggeman approximation (Sokolik

531   and Toon, 1999; Lafon et al., 2006; Koven and Fung, 2006; Mishra and Tripathi, 2008; Thomas

532   and Gautier, 2009; McConnell et al., 2010; Klaver et al., 2011a; Wagner et al., 2012; Mishra et al.,

533   2012) has been more often used for calculating the complex refractive index of silicate-hematite

534   mixtures than the Maxwell-Garnet approximations (Balkanski et al., 2007; Hansell Jr et al., 2011).

535   The Bruggeman approximation allows for the calculation of an effective dielectric constant

536   of multicomponent mixtures without distinguishing between matrix and inclusions. If we do not

537   know which is the main body for the silicate and the hematite in an aerosol, it is better to choose

the Bruggeman approximation. For the Maxwell-Garnet approximation a decision must be made as to which component is the matrix and which is an inclusion. The Maxwell-Garnett approximation is designed for small inclusions inside a host matrix and thus it is not suitable for hematite >50% in the mixture, so the calculated SSAs show abnormal fluctuation for hematite >50% in Figure 5. This phenomenon disappears if we consider the inverse Maxwell-Garnet approximation which makes hematite the host matrix. Actually, the variation of Fe_2O_3 has been constrained within the range 0–10%, so we advise the use of the Maxwell-Garnet approximation in which the inclusions should be identical in composition but may be different in volume, shape and orientation.

The comparison between the laboratories measured SSAs with known abundance of iron-oxides with our theoretically calculated SSAs by different mixing rules, would give us further insights into the actual mixing states of iron oxides and accuracy of different refractive indices. Laboratory measured SSAs by extinction and photoacoustic absorption measurements at different wavelengths have been specific reported (Linke et al., 2006; Moosmüller et al., 2012). Moosmüller et al (2012) has demonstrated that SSAs are much smaller at 405 nm than at 870 nm and all SSAs are linearly correlated with the iron content. These measured results are shown in Figure 5 for comparison with our theoretically calculated SSAs. The measured SSAs at 405 nm show good agreement with our external mixing SSA values calculated from both LG1988 and QE1985 for the abundance of hematite less than 10%, while they are much larger than our internal mixing SSA values at 405nm (Figure 5a), potentially indicating that the dust samples are mainly external mixing and are accompanied by a very small degree of internal mixing.

In contrast, the measured SSA values at 870 nm are much larger than our external and internal mixing SSA values calculated from refractive indices from QE1985 but show good agreement with our external mixing SSA values calculated using LG1988 values (Figure 5b). This illustrates the fact that the complex refractive indices of hematite from QE1985 have greatly overestimated absorption at 870 nm.
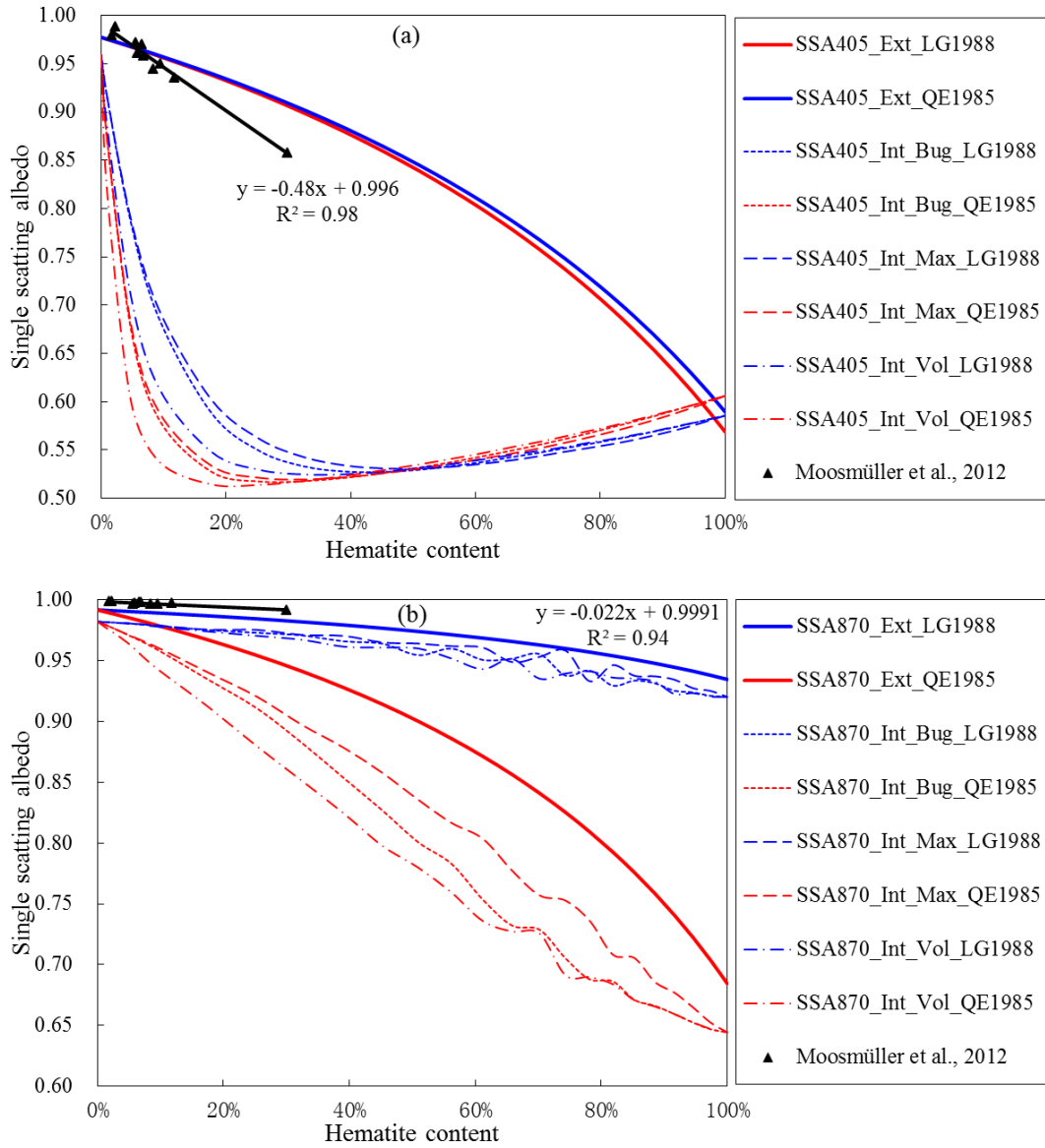
Fig. 5. The single scattering albedo (SSA) as a function of varying hematite content at wavelengths of (a) 405 and (b) 870 nm, with different mixing states (Internal and External mixing), different complex refractive index sources (QE1985 and LG1988) and mixing approximations (Volume, Maxwell-Garnet and Bruggeman). For comparison, the measured values using a photoacoustic instrument with integrating reciprocal nephelometer and linear fits from Moosmüller et al.(2012) are also shown.

For purposes of further quantitatively illustrating the optical effects of hematite to the mixtures, we calculate $\Delta\omega_0$ as the difference between the single scattering albedo of mixtures with given abundances of hematite and pure illite. Thus, we have

$$\Delta\omega_0 = \frac{\omega_0^{mixture} - \omega_0^{illite}}{\omega_0^{illite}} \times 100\% .$$

Here, we assume $M_0 = 100\,\mu g/cm^3$ and a lognormal size distribution with $r_0 = 0.5\ \mu m$, $\sigma =$

576   2.0. The single scattering albedo of pure illite represents the case when the dust contains no

577   hematite. If the calculated values of $\Delta\omega_0$ are negative, this means that hematite has high

578   absorption at the corresponding wavelengths. Figure 6 shows the calculated $\Delta\omega_0$ for hematite

579   with refractive indices from QE1985 and LG1988 at $\lambda < 20$ μm. It demonstrates that hematite

580   with refractive indices from LG1988 only enhances the optical absorption of dust mixtures for $\lambda <$

581   0.55 μm, but hematite with refractive indices from QE1985 enhances the absorption for $\lambda < 2.5$

582   μm. The magnitude of $\Delta\omega_0$ for 5% hematite over these wavelengths is approximately about 1%.

583   Therefore, the use of refractive indices for hematite from QE1985 in climate models would lead to

584   overestimation of the optical absorption at both visible and near-IR wavelengths. Another apparent

585   difference is the positive magnitude of $\Delta\omega_0$ for hematite with refractive indices from the two

586   datasets at wavelengths of $2.5 < \lambda < 8.7$ μm.

587   As about 87% of solar spectral irradiance is distributed at wavelengths from 0.4 μm to 2.5

588   μm (ASTM G-173, http://rredc.nrel.gov/solar/spectra/am1.5/), hematite with refractive indices

589   from LG1988 shows approximately equal absorption to the clay mineral illite over the whole

590   region from 0.2 μm to 2.5 μm, and only enhances the optical absorption of aerosol mixtures at $\lambda <$

591   0.55 μm. Thus, a more precise description of the nature of clays and iron oxides is necessary at

592   lower wavelengths because of large differences in their spectral optical properties.
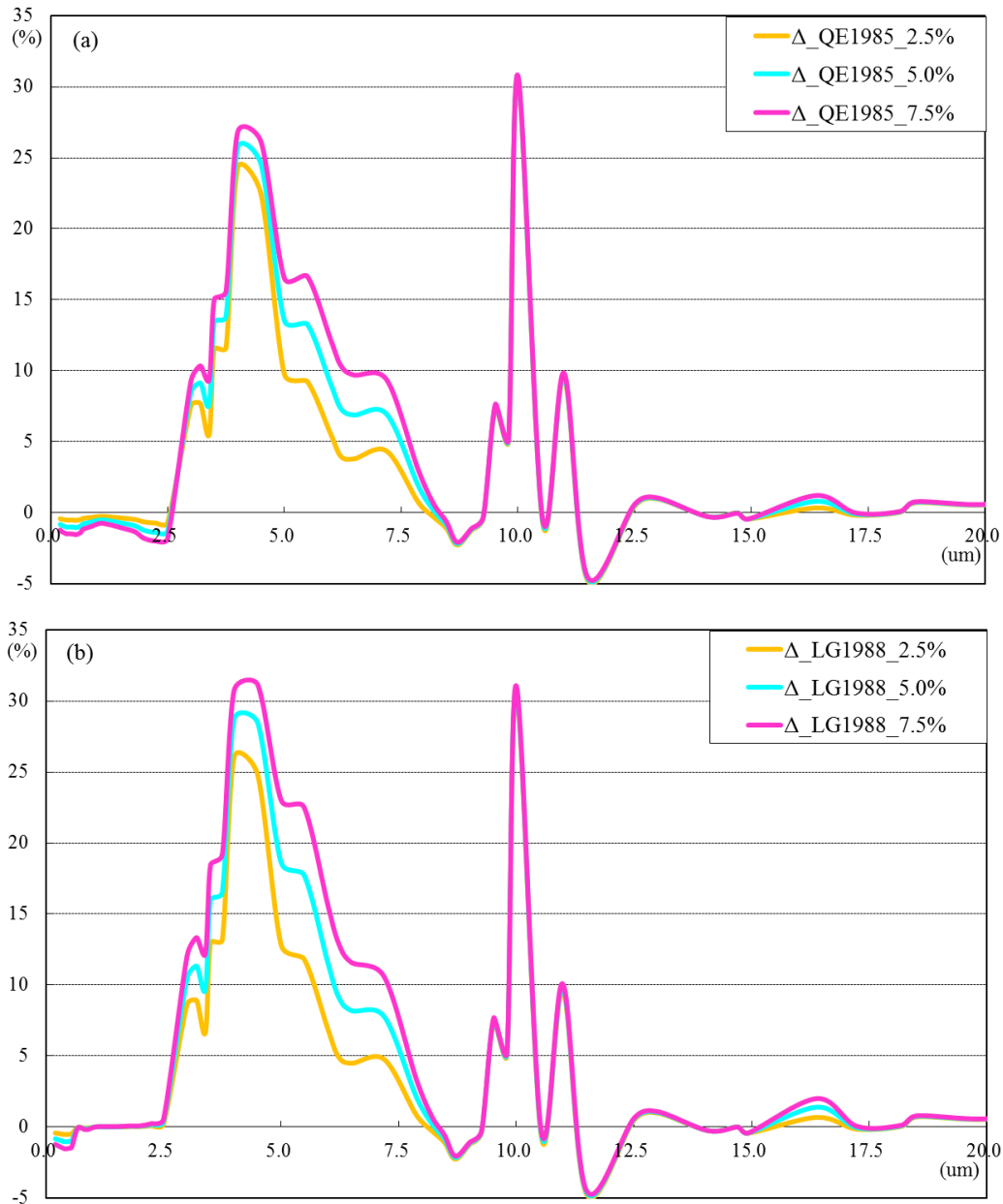
Fig. 6. The difference $\Delta\omega_0$ between the single scattering albedo (SSA) of pure illite and the single scattering albedo of mixtures with different contents and refractive indices of hematite. (a) Complex refractive index of hematite from Qurrey (1985), (b) Complex refractive index of hematite from Longtin (1988).

Given all that, the complex refractive index of iron-oxides is therefore a key parameter in effects of dust aerosols on the radiation balance, and the optical constants of hematite from different sources become a major source of uncertainty in radiative forcing calculation. Further work is needed to provide experimental measurements of the refractive index of iron-oxides, especially for hematite and goethite in the visible region of the spectrum. More complete knowledge of the dust mineralogy, morphology and size distribution with varied multi-modes is

604 needed as input to more rigorous modeling.

605

606 **4. Summary**

607 In this paper we have investigated the spectral optical properties of iron-oxides with

608 considering different refractive indices, size distributions, and more logical weight fractions and

609 mixing states of iron-oxides. The iron-oxides account for approximately half of the mass of

610 elemental Fe and for between 2 and 5 % of the dust mass. Most of them are composed of goethite,

611 representing between 50 and 75 % of the iron oxide mass. The iron-oxides commonly occur as

612 spheroidal to ellipsoidal nanoparticles that may be single or aggregated, and may be unattached or

613 attached to quartz or clay minerals, which could be expressed as semi-external mixing state.

614 Moreover, the spectral SSA values determined in the present study show a strong

615 wavelength-dependence with a steep decrease from the visible to the near-UV. There are still

616 problems that need to be solved in order to accurately study the real role of iron-oxides in

617 determining the overall impact of dust aerosols on climate perturbation, as follows:

618 1. Although there have been many published investigations of the complex refractive index of

619 different iron-oxides, uniformly continuous optical constants for a single type of iron-oxides from

620 0.2 um to 50 μm are very scarce. Some of them are inconsistent and careful checking of their

621 accuracy is therefore essential.

622 2. The abundance of specific iron-oxide types (such as goethite and magnetite) remains

623 unknown. Although many studies have measured the mass ratio of goethite to hematite as about

624 7:3, the absence of goethite optical constants at 0.75-8.5 μm restricts the usefulness of this ratio.

625 Thus, using hematite to represent all types of iron-oxides is a popular hypothesis.

626 3. Microscopic observations and optical simulations have shown that semi-external mixtures

627 employing both external mixtures of Fe-aggregates and other minerals and partly internal mixing

628 between iron-oxides and aluminosilicate particles is the optimal mixing approximation.

629 4. For hematite, there are two datasets of complex refractive indices that differ significantly.

630 Compared with LG1988, the complex refractive indices of QE1985 greatly overestimate the

631 optical absorption at both visible and near-IR wavelengths. Comprehensive laboratory

632 measurements of the refractive indices of iron-oxides, especially of hematite and goethite in the

633 visible spectrum, should therefore be made in order to accurately assess the effect of mineral dust

634   on climate perturbation.

635   Theoretically calculated SSA values are comparable to values observed in recent laboratory

636   and field studies in the range of 0.97-0.99. The iron oxide content alone cannot explain the

637   variability of the single scattering albedo, and the lower SSAs could be explained as the presence

638   of coarse dust particles and high-absorbing black carbon in natural transported dust aerosol. More

639   complete knowledge of the dust mineralogical composition and size distribution with dynamic

640   varied multi-modes is needed as input to more rigorous modeling.

641

647

648 **References**

649 Alfaro, S., Lafon, S., Rajot, J., Formenti, P., Gaudichet, A., and Maille, M.: Iron oxides and light
650   absorption by pure desert dust: an experimental study, J. Geophys. Res.-Atmos., 109, D08208,
651   doi:10.1029/2003JD004374, 2004.

652 Anderson, B. and Jenne, E.: Free-iron and-manganese oxide content of reference clays, Soil Sci., 109,
653   163–169, 1970. Angel, B. and Vincent, W.: Associated with the surface of kaolins, Clay Clay Miner.,
654   26, 263–272, 1978.

655 Arimoto, R., Balsam, W., and Schloesslin, C.: Visible spectroscopy of aerosol particles collected on
656   filters: iron-oxide minerals, Atmos. Environ., 36, 89–96, 2002.

657 Arimoto, R., Ray, B., Lewis, N., Tomza, U., and Duce, R.: Mass–particle size distributions of
658   atmospheric dust and the dry deposition of dust to the remote ocean, J. Geophys. Res. -Atmos., 102,
659   15867–15874, 1997.

660 Balkanski, Y., Schulz, M., Claquin, T., and Guibert, S.: Reevaluation of Mineral aerosol radiative
661   forcings suggests a better agreement with satellite and AERONET data, Atmos. Chem. Phys., 7, 81–
662   95, doi:10.5194/acp-7-81-2007, 2007.

663 Balsam, W., Ji, J., Renock, D., Deaton, B. C., and Williams, E.: Determining hematite content from
664   NUV/Vis/NIR spectra: limits of detection, Am. Mineral., 99, 2280–2291, 2014.

665 Baltrusaitis, J., Cwiertny, D. M., and Grassian, V. H.: Adsorption of sulfur dioxide on hematite and
666   goethite particle surfaces, Phys. Chem. Chem. Phys., 9, 5542–5554, 2007.

667 Bedidi, A. and Cervelle, B.: Light scattering by spherical particles with hematite and goethitelike
668   optical properties: effect of water impregnation, J. Geophys. Res.-Sol. Ea., 98, 11941–11952, 1993.

669 Bohren, C. F. and Huffman, D. R.: Absorption and Scattering of Light by Small Particles, John Wiley
670   and Sons, New York, 1998.

Claquin, T., Schulz, M., Balkanski, Y. J.: Modeling the mineralogy of atmospheric dust sources, J. Geophys. Res. -Atmos., 104(D18), 22243-22256, doi:10.1029/1999JD900416, 1999.

Chiapello, I., Bergametti, G., Chatenet, B., Bousquet, P., Dulac, F., and Soares, E. S.: Origins of African dust transported over the northeastern tropical Atlantic, J. Geophys. Res.-Atmos., 102, 13701–13709, 1997.

Chou, C., Formenti, P., Maille, M., Ausset, P., Helas, G., Harrison, M., and Osborne, S.: Size distribution, shape, and composition of mineral dust aerosols collected during the African monsoon multidisciplinary analysis special observation period 0: dust and biomass – burning experiment field campaign in Niger, January 2006, J. Geophys. Res.-Atmos., 113, D00C10, doi:10.1029/2008JD009897, 2008.

Chyylek, P., Srivastava, V., Pinnick, R. G., and Wang, R.: Scattering of electromagnetic waves ´by composite spherical particles: experiment and effective medium approximations, Appl. Optics, 27, 2396–2404, 1988.

Cornell, R. M. and Schwertmann, U.: The Iron Oxides: Structure, Properties, Reactions, Occurrences and Uses, John Wiley and Sons, New York, 2006.

Dang, C. and Hegg, D. A.: Quantifying light absorption by organic carbon in western North American snow by serial chemical extractions, J. Geophys. Res.-Atmos., 119, 10247–210261, 2014.

Dave, J. and Center, I. P. A. S.: Subroutines for Computing the Parameters of the Electromagnetic Radiation Scattered by a Sphere, IBM Scientific Center, Palo Alto, California, 1968.

Deboudt, K., Gloter, A., Mussi, A., and Flament, P.: Red–speciation and mixing state of iron in individual African dust particles, J. Geophys. Res.-Atmos., 117, D12307, doi:10.1029/2011JD017298, 2012.

Derimian, Y., Karnieli, A., Kaufman, Y. J., Andreae, M. O., Andreae, T. W., Dubovik, O., Maenhaut, W., and Koren, I.: The role of iron and black carbon in aerosol light absorption, Atmos. Chem. Phys., 8, 3623–3637, doi:10.5194/acp-8-3623-2008, 2008.

Dupart, Y., King, S. M., Nekat, B., Nowak, A., Wiedensohler, A., Herrmann, H., David, G., Thomas, B., Miffre, A., and Rairoux, P.: Mineral dust photochemistry induces nucleation events in the presence of SO2 , P. Natl. Acad. Sci. USA, 109, 20842–20847, 2012.

Ebert, M., Weinbruch, S., Hoffmann, P., and Ortner, H. M.: The chemical composition and complex refractive index of rural and urban influenced aerosols determined by individual particle analysis, Atmos. Environ., 38, 6531–6545, 2004.

Formenti, P., Rajot, J. L., Desboeufs, K., Caquineau, S., Chevaillier, S., Nava, S., Gaudichet, A., Journet, E., Triquet, S., and Alfaro, S.: Regional variability of the composition of mineral dust from western Africa: results from the AMMA SOP0/DABEX and DODO field campaigns, J. Geophys. Res.-Atmos., 113, D00C13, doi:10.1029/2008JD009903, 2008.

Formenti, P., Schütz, L., Balkanski, Y., Desboeufs, K., Ebert, M., Kandler, K., Petzold, A., Scheuvens, D., Weinbruch, S., and Zhang, D.: Recent progress in understanding physical and chemical properties of African and Asian mineral dust, Atmos. Chem. Phys., 11, 8231– 8256, doi:10.5194/acp-11-8231-2011, 2011.

Formenti, P., Caquineau, S., Chevaillier, S., Klaver, A., Desboeufs, K., Rajot, J., Belin, S., and Briois, V.: Dominance of goethite over hematite in iron oxides of mineral dust from Western Africa: quantitative partitioning by X-ray absorption spectroscopy, J. Geophys. Res.-Atmos., 119, 12740–12754, doi:10.1002/2014JD021668, 2014a.

Formenti, P., Caquineau, S., Desboeufs, K., Klaver, A., Chevaillier, S., Journet, E., and Rajot, J.:

Mapping the physic-chemical properties of mineral dust in western Africa: mineralogical composition, Atmos. Chem. Phys., 14, 10663–10686, doi:10.5194/acp-14-10663-2014, 2014b.

Galuza, A., Eremenko, V., and Kirichenko, A.: Analysis of hematite reflection spectrum by the Kramers–Kronig method, Sov. Phys. Solod State, 21, 654–656, 1979.

Ganor, E. and Foner, H.: The mineralogical and chemical properties and the behaviour of aeolian Saharan dust over Israel, in: The Impact of Desert Dust Across the Mediterranean, Springer, Kluwer Academic Publishers, Dordrecht, the Netherlands, 163–172, 1996.

Gao, Y., Kaufman, Y., Tanre, D., Kolber, D., and Falkowski, P.: Seasonal distributions of aeolian iron fluxes to the global ocean, Geophys. Res. Lett., 28, 29–32, 2001.

Gillespie, J. B. and Lindberg, J. D.: Ultraviolet and visible imaginary refractive index of strongly absorbing atmospheric particulate matter, Appl. Optics, 31, 2112–2115, 1992.

Ginot, P., Dumont, M., Lim, S., Patris, N., Taupin, J.-D., Wagnon, P., Gilbert, A., Arnaud, Y., Marinoni, A., Bonasoni, P., and Laj, P.: A 10 year record of black carbon and dust from a Mera Peak ice core (Nepal): variability and potential impact on melting of Himalayan glaciers, The Cryosphere, 8, 1479–1496, doi:10.5194/tc-8-1479-2014, 2014.

Glotch, T. D. and Rogers, A. D.: Evidence for aqueous deposition of hematite- and sulfate- rich 30 light-toned layered deposits in Aureum and Iani Chaos, Mars, J. Geophys. Res.-Planet., 112, E06001, doi:10.1029/2006JE002863, 2007.

Glotch, T. D. and Rossman, G. R.: Mid-infrared reflectance spectra and optical constants of six iron oxide/oxyhydroxide phases, Icarus, 204, 663–671, 2009.

Gomes, L. and Gillette, D. A.: A comparison of characteristics of aerosol from dust storms in central Asia with soil-derived dust from other regions, Atmos. Environ. A-Gen., 27, 2539–2544, 1993.

Greenland, D. J., Oades, J., and Sherwin, T.: Elecrron-microscope observations of iron oxides in some red soils, J. Soil Sci., 19, 123–126, 1968.

Guieu, C., Loÿ-Pilot, M. D., Ridame, C., and Thomas, C.: Chemical characterization of the Saharan dust end-member: some biogeochemical implications for the western Mediterranean Sea, J. Geophys. Res.-Atmos., 107, ACH 5-1–ACH 5–11, 2002.

Guo, H. and Barnard, A. S.: Naturally occurring iron oxide nanoparticles: morphology, surface chemistry and environmental stability, J. Mater. Chem., 1, 27–42, 2013.

Hansell Jr., R. A., Reid, J. S., Tsay, S. C., Roush, T. L., and Kalashnikova, O. V.: A sensitivity study on the effects of particle chemistry, asphericity and size on the mass extinction efficiency of mineral dust in the earth's atmosphere: from the near to thermal IR, Atmos. Chem. Phys., 11, 1527–1547, doi:10.5194/acp-11-1527-2011, 2011.

Haywood, J., Francis, P., Glew M., and Taylor, J.: Optical properties and direct radiative effect of Saharan dust: A case study of two Saharan dust outbreaks using aircraft data, J. Geophys. Res.-Atmos., 106(D16), 18417-18430, doi:10.1029/2000JD900319, 2001.

Haywood, J., Francis, P., Osborne, S., Glew, M., Loeb, N., Highwood, E., Tanré, D., Myhre, G., Formenti, P., and Hirst, E.: Radiative properties and direct radiative effect of Saharan dust measured by the C-130 aircraft during SHADE: 1. Solar spectrum, J. Geophys. Res.-Atmos., 108(D18), 8577, doi:10.1029/2002JD002687, 2003.

Haywood, J., Johnson, B., Osborne, S., Baran, A., Brooks, M., Milton, S., Mulcahy, J., Walters, D., Allan, R., and Klaver, A.: Motivation, rationale and key results from the GERBILS Saharan dust measurement campaign, Q. J. Roy. Meteor. Soc., 137, 1106–1116, 2011.

Henning, T. and Mutschke, H.: Low-temperature infrared properties of cosmic dust analogues, Astron.

759   Astrophys., 327, 743–754, 1997.

760 Henning, T., Begemann, B., Mutschke. H., and Dorschner, J.: Optical properties of oxide dust grains,
761   Astron. Astrophys. Sup., 112, 143–149, 1995.

762 Hinds, W. C.: Aerosol Technology: Properties, Behavior, and Measurement of Airborne Particles,
763   Wiley-Interscience, New York, 442 p., 1, 1982.

764 Höller, R., Ito, K., Tohno, S., and Kasahara, M.: Wavelength-dependent aerosol singlescattering albedo:
765   measurements and model calculations for a coastal site near the Sea of Japan during ACE-Asia, J.
766   Geophys. Res.-Atmos., 108, 8648, doi:10.1029/2002JD003250, 2003.

767 Hsu, W. P. and Matijević, E.: Optical properties of monodispersed hematite hydrosols, Appl. Optics, 24,
768   1623–1630, 1985.

769 Jeong, M. J., Tsay, S. C., Ji, Q., Hsu, N. C., Hansell, R. A., and Lee, J.: Ground-based measurements of
770   airborne Saharan dust in marine environment during the NAMMA field experiment, Geophys. Res.
771   Lett., 35, L20805, doi:10.1029/2008GL035587,2008.

772 Jickells, T., An, Z., Andersen, K. K., Baker, A., Bergametti, G., Brooks, N., Cao, J., Boyd, P., Duce, R.,
773   and Hunter, K.: Global iron connections between desert dust, ocean biogeochemistry, and climate,
774   Science, 308, 67–71, 2005.

775 Johnson, B. and Osborne, S.: Physical and optical properties of mineral dust aerosol measured by
776   aircraft during the GERBILS campaign, Q. J. Roy. Meteor. Soc., 137, 1117–1130, 2011.

777 Journet, E., Balkanski, Y., and Harrison, S. P.: A new data set of soil mineralogy for dust-cycle
778   modeling, Atmos. Chem. Phys., 14, 3801–3816, doi:10.5194/acp-14-3801-2014, 2014.

779 Kandler, K., Benker, N., Bundke, U., Cuevas, E., Ebert, M., Knippertz, P., Rodríguez, S., Schütz, L.,
780   and Weinbruch, S.: Chemical composition and complex refractive index of Saharan Mineral Dust at
781   Izana, Tenerife (Spain) derived by electron microscopy, Atmos. Environ., 41, 8058–8074, 2007.

782 Kandler, K., Schütz, L., Deutscher, C., Ebert, M., Hofmann, H., Jäckel, S., Jaenicke, R., Knippertz, P.,
783   Lieke, K., and Massling, A.: Size distribution, mass concentration, chemical and mineralogical
784   composition and derived optical parameters of the boundary layer aerosol at Tinfou, Morocco,
785   during SAMUM 2006, Tellus B, 61, 32–50, 2009.

786 Kandler, K., Lieke, K., Benker, N., Emmel, C., Küpper, M., Müller-Ebert, D., Ebert, M., Scheuvens, D.,
787   Schladitz, A., and Schütz, L.: Electron microscopy of particles collected at Praia, Cape Verde,
788   during the Saharan mineral dust experiment: particle chemistry, shape, mixing state and complex
789   refractive index, Tellus B, 63, 475–496, 2011.

790 Kang, S., Hwang, H., Kang, S., Park, Y., Kim, H., and Ro, C.-U.: Quantitative ED-EPMA combined
791   with morphological information for the characterization of individual aerosol particles collected in
792   Incheon, Korea, Atmos. Environ., 43, 3445–3453, 2009.

793 Kaspari, S., Painter, T. H., Gysel, M., Skiles, S. M., and Schwikowski, M.: Seasonal and elevational
794   variations of black carbon and dust in snow and ice in the Solu-Khumbu, Nepal and estimated
795   radiative forcings, Atmos. Chem. Phys., 14, 8089–8103, doi:10.5194/acp-14- 8089-2014, 2014.

796 Kerker, M., Scheiner, P., Cooke, D., and Kratohvil, J.: Absorption index and color of colloidal hematite,
797   J. Colloid Interf. Sci., 71, 176–187, 1979.

798 Kim, D., Chin, M., Yu, H., Eck, T. F., Sinyuk, A., Smirnov, A., and Holben, B.: Dust optical properties
799   over North Africa and Arabian Peninsula derived from the AERONET dataset, Atmos. Chem. Phys.,
800   11(20), 10733-10741, 2011.

801 Klaver, A., Formenti, P., Caquineau, S., Chevaillier, S., Ausset, P., Calzolai, G., Osborne, S., Johnson,
802   B., Harrison, M., and Dubovik, O.: Physico-chemical and optical properties of Sahelian and

803   Saharan mineral dust: in situ measurements during the GERBILS campaign, Q. J. Roy. Meteor. Soc.,
804   137, 1193–1210, 2011a.

805   Klaver, Y., Lemmens, V., Creemers, G., Rutten, H., Nienhuijs, S., and de Hingh, I.: Populationbased
806   survival of patients with peritoneal carcinomatosis from colorectal origin in the era of increasing
807   use of palliative chemotherapy, Ann. Oncol., 22, 2250–2256, 2011b.

808   Koven, C. D. and Fung, I.: Inferring dust composition from wavelength-dependent absorption in
809   Aerosol Robotic Network (AERONET) data, J. Geophys. Res.-Atmos., 111, D14205,
810   doi:10.1029/2005JD006678, 2006.

811   Köhler, C. H., Trautmann, T., Lindermeir, E., Vreeling, W., Lieke, K., Kandler, K., Weinzierl, B., Groß,
812   S., Tesche, M., and Wendisch, M.: Thermal IR radiative properties of mixed mineral dust and
813   biomass aerosol during SAMUM-2, Tellus B, 63, 751–769, 2011.

814   Krekov, G. M.: Models of atmospheric aerosols, in: Aerosol Effects on Climate, edited by: Jennings, S.
815   G., Univ. of Ariz. Press, Tucson, 9–72, 1992.

816   Lázaro, F. J., Gutiérrez, L., Barrón, V., and Gelado, M. D.: The speciation of iron in desert dust
817   collected in Gran Canaria (Canary Islands): combined chemical, magnetic and optical analysis,
818   Atmos. Environ., 42, 8987–8996, 2008.

819   Lack, D. A., Quinn, P. K., Massoli, P., Bates, T. S., Coffman, D., Covert, D. S., Sierau, B., Tucker, S.,
820   Baynard, T., Lovejoy, E., Murphy, D. M., and Ravishankara, A. R.: Relative humidity dependence
821   of light absorption by mineral dust after long-range atmospheric transport from the Sahara,
822   Geophys. Res. Lett., 36, L24805, doi:10.1029/2009GL041002, 2009.

823   Lafon, M., Megret, F., Lafage, M., and Prehaud, C.: The innate immune facet of brain, J. Mol.
824   Neurosci., 29, 185–194, 2006.

825   Lafon, S., Rajot, J.-L., Alfaro, S. C., and Gaudichet, A.: Quantification of iron oxides in desert aerosol,
826   Atmos. Environ., 38, 1211–1218, 2004.

827   Lawrence, C. R., Painter, T., Landry, C., and Neff, J.: Contemporary geochemical composition and flux
828   of aeolian dust to the San Juan Mountains, Colorado, United States, J. Geophys. Res.-Biogeo., 115,
829   G03007, doi:10.1029/2009JG001077, 2010.

830   Levoni, C., Cervino, M., Guzzi, R., and Torricella, F.: Atmospheric aerosol optical properties: a
831   database of radiative characteristics for different components and classes, Appl. Optics, 36, 8031–
832   8041, 1997.

833   Liao, H., Seinfeld, J. H.: Radiative forcing by mineral dust aerosols: sensitivity to key variables, J.
834   Geophys. Res.-Atmos., 103(D24), 31637-31645,doi:10.1029/1998JD200036, 1998.

835   Linke, C., Möhler, O., Veres, A., Mohácsi, Á., Bozóki, Z., Szabó, G., and Schnaiter, M.: Optical
836   properties and mineralogical composition of different Saharan mineral dust samples: a laboratory
837   study, Atmos. Chem. Phys., 6, 3315–3323, doi:10.5194/acp-6-3315-2006, 2006.

838   Longtin, D. R., Shettle, E. P., Hummel, J. R., and Pryce, J. D.: A Wind Dependent Desert Aerosol
839   Model: Radiative Properties, Air Force Geophys. Lab., Air Force Syst. Command Hanscom Air
840   Force Base, Mass, AFGL-TR-88-0112, 115, 1988.

841   Lu, H., Wei, W., Liu, M., Wu, X., Mou, S., and Han, Q.: Quantification and semi-quantification of
842   iron-oxide minerals in aerosol particles in the hinterland of Taklimakan Desert, Scientia
843   Geographica Sinica, 31, 969–975, 2011.

844   Mahowald, N., Albani, S., Kok, J. F., Engelstaeder, S., Scanza, R., Ward, D. S., and Flanner, M. G.: The
845   size distribution of desert dust aerosols and its impact on the Earth system, Aeolian Res., 15, 53–71,
846   2013.

Malek, M. A., Kim, B., Jung, H.-J., Song, Y.-C., and Ro, C.-U.: Single-particle mineralogy of Chinese soil particles by the combined use of low-Z particle electron probe X-ray microanalysis and attenuated total reflectance-FT-IR imaging techniques, Anal. Chem., 83, 7970–7977, 2011.

Marra, A., Blanco, A., Fonti, S., Jurewicz, A., and Orofino, V.: Fine hematite particles of Martian interest: absorption spectra and optical constants, J. Phys. Conf. Ser., 6, 132–138, 2005,.

McConnell, C. L., Formenti, P., Highwood, E. J., and Harrison, M. A. J.: Using aircraft measurements to determine the refractive index of Saharan dust during the DODO Experiments, Atmos. Chem. Phys., 10, 3081–3098, doi:10.5194/acp-10-3081-2010, 2010.

Meland, B., Kleiber, P., Grassian, V., and Young, M.: Visible light scattering study at 470, 550, and 660 nm of components of mineral dust aerosol: hematite and goethite, J. Quant. Spectrosc. Ra., 112, 1108–1118, 2011.

Menéndez, I., Pérez-Chacón, E., Mangas, J., Tauler, E., Engelbrecht, J. P., Derbyshire, E., Cana, L., and Alonso, I.: Dust deposits on La Graciosa Island (Canary Islands, Spain): texture, mineralogy and a case study of recent dust plume transport, Catena, 117, 133–144, 2014.

Mishchenko, M. I., Travis, L. D., and Lacis, A. A.: Scattering, Absorption, and Emission of Light by Small Particles, Cambridge University Press, 2002.

Mishra, S. K., Tripathi, S. N., Aggarwal, S. G., and Arola, A.: Optical properties of accumulation mode, polluted mineral dust: effects of particle shape, hematite content and semi-external mixing with carbonaceous species, Tellus B, 64, 18536, doi:10.3402/tellusb.v64i0.18536, 2012.

Mishra, S. K. and Tripathi, S. N.: Modeling optical properties of mineral dust over the Indian Desert, J. Geophys. Res.-Atmos., 113, D23201, doi:10.1029/2008JD010048, 2008.

Moosmüller, H., Engelbrecht, J. P., Skiba, M., Frey, G., Chakrabarty, R. K., and Arnott, W. P.: Single scattering albedo of fine mineral dust aerosols controlled by iron concentration, J. Geophys. Res.-Atmos., 117, D11210, doi:10.1029/2011JD016909, 2012.

Mukai, T.: Cometary dust and interplanetary particles, in: Evolution of Interstellar Dust and Related Topics, Elsevier Science, Amsterdam, 397–445, 1989.

Müller, T., Schladitz, A., Massling, A., Kaaden, N., Kandler, K., and Wiedensohler, A.: Spectral absorption coefficients and imaginary parts of refractive indices of Saharan dust during SAMUM-1, Tellus B, 61, 79–95, 2009.

Müller, T., Schladitz, A., Kandler, K., and Wiedensohler, A.: Spectral particle absorption coefficients, single scattering albedos and imaginary parts of refractive indices from ground based in situ measurements at Cape Verde Island during SAMUM-2, Tellus B, 63(4), 573-588, 2011,.

Muñoz, O., Volten, H., Hovenier, J., Min, M., Shkuratov, Y. G., Jalava, J., Van der Zande, W., and Waters, L.: Experimental and computational study of light scattering by irregular particles with extreme refractive indices: hematite and rutile, Astron. Astrophys., 446, 525–535, 2006.

Nickovic, S., Vukovic, A., Vujadinovic, M., Djurdjevic, V., and Pejanovic, G.: Technical Note: High-resolution mineralogical database of dust-productive soils for atmospheric dust modeling, Atmos. Chem. Phys., 12, 845–855, doi:10.5194/acp-12-845-2012, 2012.

Nickovic, S., Vukovic, A., and Vujadinovic, M.: Atmospheric processing of iron carried by mineral dust, Atmos. Chem. Phys., 13, 9169–9181, doi:10.5194/acp-13-9169-2013, 2013.

Onari, S., Arai, T., and Kudo, K.: Infrared lattice vibrations and dielectric dispersion in α-Fe2O3 , Phys. Rev. B, 16, 1717–1721, 1977.

Osborne, S. R., Johnson, B. T., Haywood, J. M., Baran, A. J., Harrison M. A. J., and McConnell, C. L.: Physical and optical properties of mineral dust aerosol during the Dust and Biomass-burning

891   Experiment, J. Geophys. Res.-Atmos., 113, D00C03, doi:10.1029/2007JD009551, 2008.

892   Otto, S., Bierwirth, E., Weinzierl, B., Kandler, K., Esselborn, M., Tesche, M., Schladitz, A., Wendisch,

893   M., and Trautmann, T.: Solar radiative effects of a Saharan dust plume observed during SAMUM

894   assuming spheroidal model particles, Tellus B, 61, 270–296, 2009.

895   Painter, T. H., Deems, J. S., Belnap, J., Hamlet, A. F., Landry, C. C., and Udall, B.: Response of

896   Colorado River runoff to dust radiative forcing in snow, P. Natl. Acad. Sci. USA, 107, 17125–

897   17130, 2010.

898   Patterson, E., and Gillette, D.: Commonalities in measured size distributions for aerosols having a

899   soil-derived component, J. Geophys. Res., 82, 2074–2082, 1977.

900   Peterson, J. T.: Measurement of Atmospheric Aerosols and Infrared Radiation over Northwest India and

901   heir Relationship, PhD thesis, Dep. of Meteorol., Univ. of Wis., Madison, 1968.

902   Petzold, A., Rasp, K., Weinzierl, B., Esselborn, M., Hamburger, T., Dörnbrack, A., Kandler, K., Schütz,

903   L., Knippertz, P., and Fiebig, M.: Saharan dust absorption and refractive index from aircraft-based

904   observations during SAMUM 2006, Tellus B, 61, 118–130, 2009.

905   Petzold, A., Veira, A., Mund, S., Esselborn, M., Kiemle, C., Weinzierl, B., Hamburger, T., Ehret, G.,

906   Lieke, K., and Kandler, K.: Mixing of mineral dust with urban pollution aerosol over Dakar

907   (Senegal): impact on dust physico-chemical and radiative properties, Tellus B, 63(4), 619-634,

908   2011.

909   Popova, S., Tolstykh, T., and Ivlev, L.: Optical-Constants of Fe2O3 in infrared spectral region, Optika

910   Spektrosc., 954–955, 1973.

911   Postma, D. and Brockenhuus-Schack, B. S.: Diagenesis of iron in proglacial sand deposits of late-and

912   post-Weichselian age, J. Sediment. Res., 57, 1040–1053, 1987.

913   Poulton, S. W. and Canfield, D. E.: Development of a sequential extraction procedure for iron:

914   implications for iron partitioning in continentally derived particulates, Chem. Geol., 214, 209–221,

915   2005.

916   Qin, Y. and Mitchell, R. M.: Characterisation of episodic aerosol types over the Australian continent,

917   Atmos. Chem. Phys., 9, 1943–1956, doi:10.5194/acp-9-1943-2009, 2009.

918   Querry, M. R.: Optical Constants, Contractor report, US Army Chemical Research, Development and

919   Engineering Center (CRDC), Aberdeen Proving Ground, MD, 418 pp., 1985.

920   Querry, M. R.: Optical Constants of Minerals and Other Materials from the Millimeter to the

921   Ultraviolet, CRDEC-CR88009, US Army Chemical Research, Development and Engineering

922   Center, Aberdeen Proving Ground, MD, 331 pp., 1987.

923   Querry, M. R., Osborne, G., Lies, K., Jordon, R., and Coveney Jr., R. M.: Complex refractive index of

924   limestone in the visible and infrared, Appl. Optics, 17, 353–356, 1978.

925   Raiswell, R. and Anderson, T.: Reactive Iron Enrichment in Sediments Deposited Beneath Euxinic

926   Bottom Waters: Constraints on Supply by Shelf Recycling, Special Publications, Geological Society,

927   London, 248, 179–194, 2005.

928   Redmond, H. E., Dial, K. D., and Thompson, J. E.: Light scattering and absorption by wind blown dust:

929   theory, measurement, and recent data, Aeolian Res., 2, 5–26, 2010.

930   Reynolds, R. L., Goldstein, H. L., Moskowitz, B. M., Bryant, A. C., Skiles, S. M., Kokaly, R. F., Flagg,

931   C. B., Yauk, K., Berquó, T., and Breit, G.: Composition of dust deposited to snow cover in the

932   Wasatch Range (Utah, USA): controls on radiative properties of snow cover and comparison to

933   some dust-source sediments, Aeolian Res., 15, 73–90, 2013.

934   Reynolds, R. L., Cattle, S. R., Moskowitz, B. M., Goldstein, H. L., Yauk, K., Flagg, C. B., Berquó, T.

S., Kokaly, R. F., Morman, S., and Breit, G. N.: Iron oxide minerals in dust of the Red Dawn event in eastern Australia, September 2009, Aeolian Res., 15, 1–13, 2014.

Ryder, C. L., Highwood, E. J., Rosenberg, P. D., Trembath J., Brooke, J. K., Bart, M., Dean, A., Crosier, J., Dorsey, J., Brindley, H., Banks, J., Marsham, J. H., McQuaid, J. B., Sodemann, H., and Washington, R.: Optical properties of Saharan dust aerosol and contribution from the coarse mode as measured during the Fennec 2011 aircraft campaign, Atmos. Chem. Phys., 13(1), 303-325, 2013.

Scanza, R. A., Mahowald, N., Ghan, S., Zender, C. S., Kok, J. F., Liu, X., Zhang, Y., and Albani, S.: Modeling dust as component minerals in the Community Atmosphere Model: development of framework and impact on radiative forcing, Atmos. Chem. Phys., 15, 537–561, doi:10.5194/acp-15-537-2015, 2015.

Scheinost, A., Chavernas, A., Barrón, V., and Torrent, J.: Use and limitations of second-derivative diffuse reflectance spectroscopy in the visible to near-infrared range to identify and quantity fe oxide minerals in soils, Clay Clay Miner., 46, 528–536, 1998.

Scheuvens, D., Kandler, K., Küpper, M., Lieke, K., Zorn, S., Ebert, M., Schütz, L., and Weinbruch, S.: Individual–analysis of airborne dust samples collected over Morocco in 2006 during SAMUM 1, Tellus B, 63, 512–530, 2011.

Schladitz, A., Müller, T., Kaaden, N., Massling, A., Kandler, K., Ebert, M., Weinbruch, S., Deutscher, C., and Wiedensohler, A.: In situ measurements of optical properties at Tinfou (Morocco) during the Saharan mineral dust experiment SAMUM 2006, Tellus B, 61, 64–78, 2009.

Schroth, A. W., Crusius, J., Sholkovitz, E. R., and Bostick, B. C.: Iron solubility driven by speciation in dust sources to the ocean, Nat. Geosci., 2, 337–340, 2009.

Schwertmann, U.: Relations between iron oxides, soil color, and soil formation, in: Soil Science Society of America, edited by: Bigham, J. M. and Ciolkosz, E. J., Soil Color, Special Pub., Vol. 31., Madison, WI, 51–69, 1993.

Shao, Y., Wyrwoll, K.-H., Chappell, A., Huang, J., Lin, Z., McTainsh, G. H., Mikami, M., Tanaka, T. Y., Wang, X., and Yoon, S.: Dust cycle: an emerging core theme in Earth system science, Aeolian Res., 2, 181–204, 2011.

Shen, Z., Cao, J., Zhang, X., Arimoto, R., Ji, J., Balsam, W., Wang, Y., Zhang, R., and Li, X.: Spectroscopic analysis of iron-oxide minerals in aerosol particles from northern China, Sci. Total Environ., 367, 899–907, 2006.

Shettle, E. P. and Fenn, R. W.: Models for the Aerosols of the Lower atmosphere and the Effects of Humidity Variations on their Optical Properties, Environmental Research Papers, No. 676, AFGL-TR-79-0214, USAF, 94 pp., 1979.

Shi, Z., Shao, L., Jones, T., and Lu, S.: Microscopy and mineralogy of airborne particles collected during severe dust storm episodes in Beijing, China, J. Geophys. Res.-Atmos., 110, D01303, doi:10.1029/2004JD005073, 2005.

Shi, Z., Krom, M. D., Bonneville, S., Baker, A. R., Jickells, T. D., and Benning, L. G.: Formation of iron nanoparticles and increase in iron reactivity in mineral dust during simulated cloud processing, Environ. Sci. Technol., 43, 6592–6596, 2009.

Shi, Z., Bonneville, S., Krom, M. D., Carslaw, K. S., Jickells, T. D., Baker, A. R., and Benning, L. G.: Iron dissolution kinetics of mineral dust at low pH during simulated atmospheric processing, Atmos. Chem. Phys., 11, 995–1007, doi:10.5194/acp-11-995-2011, 2011.

Shi, Z., Krom, M. D., Jickells, T. D., Bonneville, S., Carslaw, K. S., Mihalopoulos, N., Baker, A. R., and Benning, L. G.: Impacts on iron solubility in the mineral dust by processes in the source region

979   and the atmosphere: a review, Aeolian Res., 5, 21–42, 2012.

980   Smith, A. J. and Grainger, R. G.: Does variation in mineral composition alter the short-wave light
981   scattering properties of desert dust aerosol?, J. Quant. Spectrosc. Ra., 133, 235–243, 2014.

982   Sokolik, I. N., Winker, D., Bergametti, G., Gillette, D., Carmichael, G., Kaufman, Y., Gomes, L.,
983   Schuetz, L., and Penner, J.: Introduction to special section: outstanding problems in quantifying the
984   radiative impacts of mineral dust, J. Geophys. Res.-Atmos., 106, 18015–18027, 2001.

985   Sokolik, I. N. and Toon, O. B.: Incorporation of mineralogical composition into models of the radiative
986   properties of mineral aerosol from UV to IR wavelengths, J. Geophys. Res.-Atmos., 104, 9423–
987   9444, 1999.

988   Song, X. and Boily, J.-F.: Carbon dioxide binding at dry FeOOH mineral surfaces: evidence for
989   structure-controlled speciation, Environ. Sci. Technol., 47, 9241–9248, 2013.

990   Steyer, T. R.: Infrared optical properties of some solids of possible interest in astronomy and
991   atmospheric physics, PhD thesis, Dep. of Phys., Univ. of Ariz., Tucson, 1974.

992   Sumner, M.: Effect of iron oxides on positive and negative charges in clays and soils, Clay Miner. Bull,
993   5, 218–226, 1963.

994   Takahashi, Y., Higashi, M., Furukawa, T., and Mitsunobu, S.: Change of iron species and iron solubility
995   in Asian dust during the long-range transport from western China to Japan, Atmos. Chem. Phys., 11,
996   11237–11252, doi:10.5194/acp-11-11237-2011, 2011.

997   Takahashi, Y., Furukawa, T., Kanai, Y., Uematsu, M., Zheng, G., and Marcus, M. A.: Seasonal changes
998   in Fe species and soluble Fe concentration in the atmosphere in the Northwest Pacific region based
999   on the analysis of aerosols collected in Tsukuba, Japan, Atmos. Chem. Phys., 13, 7695–7710,
1000   doi:10.5194/acp-13-7695-2013, 2013.

1001   Tegen, I., Hollrig, P., Chin, M., Fung, I., Jacob, D., and Penner, J.: Contribution of different aerosol
1002   species to the global aerosol extinction optical thickness: estimates from model results, J. Geophys.
1003   Res.-Atmos., 102, 23895–23915, 1997.

1004   Thomas, M. and Gautier, C.: Investigations of the March 2006 African dust storm using groundbased
1005   column-integrated high spectral resolution infrared (8–13 μm) and visible aerosol optical thickness
1006   measurements: 2. Mineral aerosol mixture analyses, J. Geophys. Res.-Atmos., 114, D14209,
1007   doi:10.1029/2008JD010931, 2009.

1008   Tipping, E.: The adsorption of aquatic humic substances by iron oxides, Geochim. Cosmochim. Ac., 45,
1009   191–199, 1981.

1010   Torrent, J. and Barrón, V.: Diffuse reflectance spectroscopy of iron oxides, in: Encyclopedia of Surface
1011   and Colloid Science, Marcel Dekker, Inc., New York, 1438–1446, 2002.

1012   Wagner, R., Ajtai, T., Kandler, K., Lieke, K., Linke, C., Müller, T., Schnaiter, M., and Vragel, M.:
1013   Complex refractive indices of Saharan dust samples at visible and near UV wavelengths: a
1014   laboratory study, Atmos. Chem. Phys., 12, 2491–2512, doi:10.5194/acp-12-2491-2012, 2012.

1015   Wijenayaka, L. A., Rubasinghege, G., Baltrusaitis, J., and Grassian, V. H.: Surface chemistry of
1016   α-FeOOH nanorods and microrods with gas-phase nitric acid and water vapor: insights into the role
1017   of particle size, surface structure, and surface hydroxyl groups in the adsorption and reactivity of
1018   α-FeOOH with atmospheric gases, J. Phys. Chem. C, 116, 12566–12577, 2012.

1019   Yang, S., Sheng, Y., Han, Y., and Chen, S.: Diffuse reflectance spectroscopic analysis of iron-oxide
1020   minerals in dust aerosol from Golmud, J. Lanzhou University (Natural Sciences), 50, 710–715,
1021   2014.

1022   Zhang, X., Gong, S., Shen, Z., Mei, F., Xi, X., Liu, L., Zhou, Z., Wang, D., Wang, Y., and Cheng, Y.:

1023   Characterization of soil dust aerosol in China and its transport and distribution during 2001
1024   ACE-Asia: 1. Network observations, J. Geophys. Res.-Atmos., 108, 4261,
1025   doi:10.1029/2002JD002632, 2003.
1026   Zhu, A., Ramanathan, V., Li, F., and Kim D.: Dust plumes over the Pacific, Indian, and Atlantic oceans:
1027   Climatology and radiative impact, J. Geophys. Res.-Atmos., 112, D16208,
1028   doi:10.1029/2007JD008427, 2007.